1 **Dense Bicoid Hubs Accentuate Binding along the Morphogen Gradient**

2 Mustafa Mir[1], Armando Reimer[2], Jenna E. Haines[1], Xiao-Yong Li[3], Michael Stadler[1], Hernan

3 Garcia[1,2,4], Michael B. Eisen[1,2,3,5], Xavier Darzacq[1,*]

4 [1]Department of Molecular and Cell Biology, University of California, Berkeley, CA, 94720,

5 USA

6 [2]Biophysics Graduate Group, University of California, Berkeley, CA, 94720, USA

7 [3]Howard Hughes Medical Institute, University of California, Berkeley, CA, 94720, USA

8 [4]Department of Physics, University of California, Berkeley, CA, 94720, USA

9 [5]Department of Integrative Biology, University of California, Berkeley, CA, 94720, USA

10 *Correspondence to: darzacq@berkeley.edu

11 **ABSTRACT**

12 Morphogen gradients direct the spatial patterning of developing embryos, however, the

13 mechanisms by which these gradients are interpreted remain elusive. Here we perform *in vivo*

14 single molecule imaging in early *Drosophila melanogaster* embryos of the transcription factor

15 Bicoid that forms a gradient and initiates patterning along the anteroposterior axis. We observe

16 that Bicoid binds to DNA with a rapid off-rate, such that its average occupancy at target loci is

17 on-rate dependent, a property required for concentration-sensitive regulation. Surprisingly, we

18 also observe abundant specific DNA binding in posterior nuclei, where Bicoid levels are

19 vanishingly low. Live embryo imaging reveals spatiotemporal "hubs" of local high Bicoid

20 concentration that are dependent on the ubiquitous maternal factor Zelda. We propose that

21 localized modulation of transcription factor on-rates via clustering, provides a general

22 mechanism to facilitate binding to low-affinity targets, and that this may be a prevalent feature

23 directing other developmental transcription networks.

24

INTRODUCTION

Spatial patterning during embryonic development is orchestrated through concentration gradients of regulatory molecules known as morphogens (Turing, 1952; Wolpert, 1969). The maternally deposited transcription factor (TF) Bicoid (BCD) in *Drosophila melanogaster* was the first identified morphogen (Driever & Nusslein-Volhard, 1988b), and remains an iconic and widely studied developmental regulator. Bicoid is distributed in an exponentially decaying concentration gradient along the anteroposterior (A-P) axis of embryos and predominantly regulates the activity of ~100 genes in distinct spatial expression domains ranging from the anterior tip to the middle of the embryo (Driever & Nusslein-Volhard, 1988a; Driever & Nussleinvolhard, 1989; Driever, Siegel, & Nusslein-Volhard, 1990; Struhl, Struhl, & Macdonald, 1989). The ability of BCD and other morphogens to activate target genes in different locations across gradients is classically thought to arise from the modulation of the number and strength of cognate DNA binding sites within target enhancers (Burz, Rivera-Pomar, Jackle, & Hanes, 1998; Lebrecht et al., 2005; H. Xu, Sepulveda, Figard, Sokac, & Golding, 2015), with sharp expression domain boundaries set through cooperative binding (Ephrussi & St Johnston, 2004; Lebrecht et al., 2005).

In recent years this classical model of concentration dependent activation has been challenged through experiments on mutant embryos with flattened BCD distributions which reveal that segment order and polarity can be maintained even without a concentration gradient (Ochoa-Espinosa, Yu, Tsirigos, Struffi, & Small, 2009). It has been suggested that instead of a pure concentration dependence, the activation of BCD target genes and the resulting sharp expression domain boundaries is tightly regulated by spatially opposing gradients of repressors (Chen, Xu, Mei, Yu, & Small, 2012) and the combinatorial actions of other transcription factors (P. Combs & Eisen, 2017). The recent discovery of the ubiquitous factor Zelda and its role in the

2

49 regulation of chromatin accessibility (Foo et al., 2014; Harrison, Li, Kaplan, Botchan, & Eisen,

50 2011; Li, Harrison, Villata, Kaplan, & Eisen, 2014; Liang et al., 2008; Schulz et al., 2015; Sun et

51 al., 2015; Z. Xu et al., 2014) and in modulating the timing and strength of Bicoid (Hannon,

52 Blythe, & Wieschaus, 2017; Z. Xu et al., 2014) and Dorsal (Foo et al., 2014) controlled enhancer

53 activation in a concentration dependent fashion has further strengthened the hypothesis

54 (Lucchetta, Lee, Fu, Patel, & Ismagilov, 2005) that the interpretation of the BCD and other

55 morphogen gradients is more complex than previously thought.

56 The validity of these models and essential mechanistic questions about how BCD, and

57 morphogens in general, differentially activate genes along a concentration gradient have been

58 challenging to resolve with current approaches. For example, extant models cannot address how

59 BCD is sufficient for activating its targets such as Knirps (Rivera-Pomar, Lu, Perrimon, Taubert,

60 & Jackle, 1995) and Hairy (La Rosee, Hader, Taubert, Rivera-Pomar, & Jackle, 1997), in the

61 posterior of the embryo, where BCD nuclear concentrations are <2nM (Morrison, Scheeler,

62 Dubuis, & Gregor, 2012) in the short interphase times (5-10 minutes) of the early nuclear cycles.

63 Since the question of how BCD molecules can find their targets in these short times requires

64 dynamic measurements, genomic assays and biochemical approaches which provide static

65 snapshots are inadequate. In this study, we address this gap in our understanding by performing

66 direct measurements of BCD-DNA interactions *in vivo* by single molecule imaging.

67 Single molecule imaging in living cells has been increasingly used in recent years to

68 measure the dynamics of TF-DNA interactions (Liu, Lavis, & Betzig, 2015). However, the

69 techniques commonly used are not suitable for whole embryos and thick tissues. Total Internal

70 Reflection (TIRF) and Highly-Inclined illumination (Hi-Lo) (Tokunaga, Imamoto, & Sakata-

71 Sogawa, 2008) which have enabled single molecule imaging in monolayer cell cultures use

72   wide-field excitation geometries and restrict the illumination volume to a small distance above

73   the microscope coverslip in order to limit the excitation of out-of-focus fluorophores. This

74   confinement of the illumination volume is necessary to achieve the signal-to-background ratios

75   (SBRs) required for single molecule detection. Consequentially, if the thickness of the

76   illumination volume is extended to image further away from the coverslip, the SBR degrades as

77   more and more out-of-focus fluorophore emission raises the background level and reduces

78   contrast. This degradation is further exacerbated when imaging highly auto- fluorescent samples

79   such as embryos or thick tissues.

80   Lattice Light-Sheet Microscopy (LLSM) was recently developed to overcome these

81   technical barriers (B. C. Chen et al., 2014). Here we apply LLSM to developing *Drosophila*

82   *melanogaster* embryos in order to characterize the single molecule DNA-binding kinetics of

83   BCD. We find that BCD binds to chromatin in a highly transient manner across the concentration

84   gradient, and were surprised to observe a significant number of binding events even at low

85   concentrations in the posterior-most regions of the embryo. Examination of the spatial

86   distribution of BCD binding events reveals spatiotemporal hubs of high local BCD

87   concentration. Through genome wide analysis of BCD-DNA binding on dissected posterior

88   segments of embryos, we show that the binding we observe via single molecule imaging in

89   posterior nuclei occurs at specific regulatory regions. We find that the regions which are

90   enriched for BCD in the posterior segments are highly correlated with Zelda (ZLD) binding,

91   signifying its role in mediating the formation of BCD hubs. Through single molecule imaging of

92   BCD in ZLD null embryos we show that ZLD is required for the formation of BCD hubs in the

93   posterior embryo. Together, these data advocate for a model in which ZLD mediates the

94   formation of hubs of high local BCD concentration and enables the activation of BCD dependent

95   targets at all position across the anteroposterior axis of the embryo.

96   **RESULTS**

97   **<u>Single molecule imaging in living Drosophila embryos using Lattice Light-Sheet</u>**

98   **<u>Microscopy</u>**

99   The principle of LLSM (Figure 1-figure supplement 1) is to create an excitation light-

100   sheet that matches the depth-of-field of the detection objective such that only fluorophores that

101   are in focus are excited (B. C. Chen et al., 2014). As in all light-sheet microscopes, in LLSM the

102   excitation and detection objectives are independent and oriented orthogonally to each other.

103   However, unlike conventional light-sheet modalities that use Gaussian beam illumination, in

104   LLSM an array of Bessel beams is used. The spacing and phase of the Bessel beams in the array

105   is controlled such that their side-lobes destructively interfere in order to achieve maximal axial

106   confinement of the light-sheet. Thus, unlike in wide-field excitation geometries the thickness of

107   the excitation volume in LLSM is independent of the distance from the coverslip which is being

108   probed. This approach enables single molecule imaging of BCD-eGFP in living *Drosophila*

109   embryos over a large field of view with high temporal resolution (Figure 1 A-B, Figure 1-figure

110   supplement 2 and Videos 1-3). We utilize a *yw*; *his2av-mrfp1; bcdE1, egfp-bcd* fly line in which

111   only the labelled BCD is expressed indicating proper functionality and expression levels

112   (Gregor, Wieschaus, McGregor, Bialek, & Tank, 2007) to ensure that all molecules we observe

113   are functionally relevant. The single molecule nature of the data is reflected in the distribution of

114   intensities (Video 2 and Figure 1-figure supplement 2A-B) and discrete characteristics (Video 2

115   and Figure 1-figure supplement 2C-D) of the observed binding events.

116   Bicoid nuclear concentrations range from ~50 nM at the anterior most positions down to

117   <2 nM (Morrison et al., 2012) in the posterior. This translates to a range on the order of 10^4-10^2

118   BCD molecules/nucleus. Assuming an isotropic distribution of molecules and a 400 nm thick

119   imaging volume, we can estimate a range on the order of 10^3-10^1 BCD molecules/ imaging

120   plane. This range of concentrations is reflected in the data shown in Video 1, where

121   unambiguous single molecule detections can be seen in the middle and posterior positions from

122   the start, whereas in the anterior positions they can only be detected when a sufficient amount of

123   bleaching has occurred. This natural concentration range allows us to perform single molecule

124   tracking at all positions in the embryo without utilizing sparse labelling strategies or photo-

125   switchable fluorophores.

126   **Bicoid binds chromatin in a highly transient manner across the concentration gradient**

127   The classical model for morphogens predicts a difference in the average dissociation rates

128   of Bicoid along the A-P axis. For example, genes that are activated at lower concentrations

129   should have higher affinity sites resulting in lower off-rates to enable a higher time-average

130   occupancy (i.e. residence time, RT). To test this model at the single molecule level we therefore

131   first performed single molecule imaging and tracking at long (100 millisecond) exposure times,

132   effectively blurring out the fast moving (unbound) population (Videos 1-2 and Figure 1-figure

133   supplement 2) (J. J. Chen et al., 2014) to estimate the residence times of BCD binding in nuclei

134   at all positions along the A-P axis.

135   Previous single molecule studies of transcription factors have consistently found two

136   populations in the survival probability distributions, a short-lived population with RTs on the

137   order of hundreds of milliseconds, and a longer-lived population with RTs on the order of 10's of

138   seconds to minutes (J. J. Chen et al., 2014; Hansen, Pustova, Cattoglio, Tjian, & Darzacq, 2017;

139 Normanno et al., 2015). These two populations have often been shown to be the non-specific and

140 specific binding populations, respectively. The survival probability distributions of BCD

141 similarly are fit better with a two-exponent model than with a single-exponent model indicating

142 the presence of two sub-populations (Figure 1- figure supplement 3 and Figure 1-figure

143 supplement 4). Fits to the survival probability distributions of BCD binding events (Figure 1C

144 and Table 1) in the anterior, middle and posterior thirds of the embryo identified short-lived

145 populations with average RTs (after photo-bleaching correction) on the order of 100s of

146 milliseconds and longer lived populations with average RTs on the order of seconds, and with no

147 significant dependence on position along the A-P axis for either population (Table 1). This

148 finding is contrary to the classical model which predicts a modulation of binding affinity as the

149 mechanism for concentration readout. The validity of our RT estimations are supported by

150 additional measurements at 500 millisecond exposure times (Figure 1-figure supplement 4).

151 Remarkably, the RT of the long-lived population is much shorter than lifetimes (10-60

152 sec) typically observed for other sequence specific DNA binding TFs using single molecule

153 tracking (J. J. Chen et al., 2014; Hansen et al., 2017). The transient nature of BCD binding is

154 further supported by Fluorescence Recovery After Photobleaching (FRAP) experiments (Figure.

155 1D) which reveal fast halftimes of recovery on the order of hundreds of milliseconds (Figure 1-

156 figure supplement 5) and previous measurements by others using Fluorescence Correlation

157 Spectroscopy (Porcher et al., 2010). The dominance of the short-lived interactions (Figure 1C)

158 highlights the preponderance of low-affinity BCD binding sites in the *Drosophila melanogaster*

159 genome and the resulting large number of non-specific interactions as previously suggested by

160 genomic studies that captured its promiscuous binding behavior (Li et al., 2008; Ochoa-Espinosa

161 et al., 2005). In addition to the expected large number of binding events in the anterior and

7

162   middle segments of the embryo, we also observed a surprisingly large number of potentially

163   specific binding events in the posterior-most nuclei where BCD has been reported to be at

164   vanishingly low (<2nM posterior vs ~50 nM anterior) concentrations (Morrison et al., 2012).

165   **Spatiotemporal hubs of Bicoid binding enrich local concentrations in the posterior embryo**

166   The lack of a detectable difference in the survival probability distributions along the A-P

167   axis and the observation of significant binding in posterior nuclei prompted us to examine how

168   much of the small BCD population remaining in the posterior embryo is actually bound vs.

169   mobile. Since longer exposure times only allow detection of molecules bound for at least the

170   span of the exposure and don't provide any data on the mobile population, we performed single

171   molecule tracking measurements at a decreased exposure time of 10 milliseconds. The signal-to-

172   noise ratios at these lower exposure times are adversely affected as expected, limiting the type of

173   analysis that can performed on this data (Video 3). However, despite this reduced contrast we

174   were able to perform single particle tracking, and through analyses of displacement distributions

175   (Figure 2 –figure supplement 1), we estimated the fraction of BCD that is bound along the A-P

176   axis (Figure. 2A). This analysis suggests that a greater fraction of the BCD population is bound

177   in more posterior positions of the embryo where BCD is present at the lowest concentrations.

178   This counter-intuitive result motivated us to further examine the 100 millisecond exposure time

179   dataset beyond the analysis of residence times described above.

180   Analyses of the spatial distribution of binding events in the 100 millisecond dataset

181   revealed a distinct clustering of binding events which becomes more pronounced toward

182   posterior positions (Figure 2B, Figure 2- figure supplement 2). Remarkably, although the number

183   of binding events per nucleus follows the trend dictated by the global concentration gradient

184   across the embryo (Figure 2C), the distribution of BCD molecules detected per cluster or "hub"

185   is maintained even in the posterior (Figure 2D). These data suggest that the formation of BCD

186   hubs with high time-averaged occupancy at specific sites in nuclei across the A-P axis is

187   conserved independent of the global concentration gradient. This surprising finding raises the

188   questions of whether the binding in the hubs observed in posterior nuclei is to specific targets

189   and whether a mechanism then exists to selectively enrich local time-averaged concentrations in

190   order to promote these interactions.

191   **Bicoid binds specific regulatory regions in the posterior embryo in a Zelda dependent**

192   **manner**

193   To test whether BCD is binding with specificity in the posterior embryo we analyzed its

194   binding profiles in a spatially segregated manner (P. A. Combs & Eisen, 2013) by comparing

195   ChIP-seq profiles derived from individually dissected posterior thirds of embryos to previously

196   published data from whole embryos (Bradley et al., 2010). Our analysis reveals that BCD indeed

197   binds to known targets in the posterior but with increased relative enrichment at specific

198   enhancer elements (Figure 3A). For example, in the *hunchback* locus, binding at the posterior

199   stripe enhancer (Perry, Bothma, Luu, & Levine, 2012) is highly enriched over the background in

200   nuclei from the dissected posterior third relative to the whole embryo. Intriguingly, genomic

201   regions that exhibit a relative increase in BCD occupancy in the posterior are correlated with an

202   enrichment of Zelda (ZLD) binding (Figure 3A and Figure 3-figure supplement 1), a ubiquitous

203   activator often described as a pioneer factor active during early embryonic development (Foo et

204   al., 2014; Harrison et al., 2011; Liang et al., 2008; Z. Xu et al., 2014). Remarkably, enrichment

205   of ZLD is more predictive of BCD binding in the posterior than previously determined position

206   of enhancer activity for the loci shown in Figure 3A. Analysis of the correlation between BCD

207   and ZLD enrichment at the cis-regulatory modules of 12 gene loci, and at ZLD and BCD peaks

208   genome-wide reveal that binding of BCD in posterior nuclei is highly correlated with ZLD co-

209   binding (Figure 3A, Figure 3-figure supplement 1, and Figure 3-figure supplement 2).

Formation of Bicoid hubs in the posterior embryo is dependent on Zelda

211   The posterior thirds genomic data and the published evidence for Zelda's role in the

212   regulation of chromatin accessibility (Foo et al., 2014; Harrison et al., 2011; Li et al., 2014;

213   Liang et al., 2008; Schulz et al., 2015; Sun et al., 2015; Z. Xu et al., 2014) and its suggested role

214   in the modulation of TF binding at low concentrations (Schulz et al., 2015; Z. Xu et al., 2014)

215   naturally led us to hypothesize that the observed clustering of BCD binding events may be, in

216   part, mediated by ZLD. We thus generated *zelda* null embryos and measured BCD binding at

217   100 millisecond exposure times, and found an abolishment of BCD hubs in the posterior embryo

218   and a small but insignificant decrease in RTs (Figure 3C, Table 1). Due to this loss of clustering

219   the same analysis that was performed in the WT case (Figure 2C) could not be done in the ZLD

220   mutants. We thus calculated the pair-correlation function for the spatial distribution of binding

221   events in both the WT and ZLD mutants (Cisse et al., 2013). This analysis allows us to infer

222   whether binding events are spatially randomly distributed or clustered (Figure 3-figure

223   supplement3). Both the magnitude and correlation length indicate a diminishment of clustering

224   in the posterior nuclei of the ZLD mutants. We also note that due to the lower labelling density

225   of BCD in the *zelda* null embryos the presumably ZLD independent clustering in the anterior

226   embryo now becomes more apparent (Figure 3-figure supplement 3). The loss of clustering in

227   the ZLD mutants also confirms that the clustering we originally observed is not due to

228   aggregation of eGFP, or other artifacts reasons.

229   Although the exact mechanism by which ZLD mediates BCD hub formation and binding

230   remains unclear, we speculate that a combination of protein-protein interactions facilitated by

231   intrinsically disordered low-complexity domains(Hamm, Bondra, & Harrison, 2015) of ZLD and

232   its reported role in promoting chromatin accessibility (Foo et al., 2014; Li et al., 2014; Schulz et

233   al., 2015; Sun et al., 2015) may contribute to BCD clustering (Figure 4).

234   **DISCUSSION**

235   Our initial observation of the low affinity nature of BCD binding to chromatin fits the

236   classical view of BCD as a concentration-dependent morphogen. We envision that high TF

237   concentrations (in the anterior embryo) potentiate rapid on-rates along with a high chromatin

238   occupancy. The observed high off-rate also suggests that BCD is free to frequently sample non-

239   specific sites (Figure 4). Thus, as BCD concentrations decrease posteriorly along the gradient,

240   there should be progressively lower on-rates and the binding at specific sites should be

241   correspondingly diminished, regardless of the roles of opposing repressor gradients. However,

242   this simplistic model essentially consigns BCD to no posterior function and contradicts a wealth

243   of evidence in the literature pointing to a specific role for BCD in the regulation of posterior

244   gene expression (Burz et al., 1998; Chen et al., 2012; La Rosee et al., 1997; Ochoa-Espinosa et

245   al., 2009; Rivera-Pomar et al., 1995; Small, Blair, & Levine, 1996). Although this paradox is

246   inexplicable under the classical morphogen model and not addressed by more recent studies that

247   cannot access dynamic information, our evidence for local high-concentration BCD "hubs"

248   capable of modulating specific binding with help from ZLD in the posterior suggests a novel

249   mechanism for TFs to carry out their regulatory role even when present at very low

250   concentrations (Figure. 4). The formation of such clusters or hubs has been reported for other

251   TFs (J. J. Chen et al., 2014; Justin Crocker et al., 2017; Liu et al., 2014) and for RNA

252   Polymerase II (Cisse et al., 2013) and indicate that such spatial organization of the nucleus may

253   be a general mechanism to catalyze important regulatory interactions. During embryonic

254   development, it is likely that clustering of TFs mediated by co-factors has evolved in eukaryotes

255   to allow exquisite spatial and segmental modulation during development through enabling

256   interactions with low-affinity enhancers (J. Crocker, Noon, & Stern, 2016).

257   **MATERIALS AND METHODS**

258   **Fly husbandry**

259   All fly cages were prepared by combining males and females of the desired strains in a plastic

260   cage left at room temperature in light at least 3 days prior to imaging. The lids on the cages were

261   filled with agar dissolved in apple juice (2.4% g/w Bacto agar, 25% apple juice, 75% distilled

262   water, and .001% of mold inhibitor from solution of 0.1g/ml (Carolina 87-6165). A paste of dry

263   yeast was smeared on the lids to induce egg laying. Lids were exchanged once each day.

264   The fly strain used for all WT BCD imaging experiments was: *yw*; *his2av-mrfp1; BcdE1,*

265   *egfp-bcd*. This fly line results in embryos where only the labelled BCD is expressed indicating

266   proper functionality and expression levels (Gregor et al., 2007). For the *zld-* experiments, *bcd-*

267   *egfp* heterozygous virgins with *zld-* germline cells (maternal germline clones prepared as in

268   (Liang et al., 2008)) were crossed to *yw* males, and progeny were used for imaging 2-3 hours

269   after laying. The heterozygosity results in only half of the BCD labelled in the *zld-* embryos. For

270   photo-bleaching controls the line used was *yw, his2av-egfp; +/+* (Bloomington # 24163).

271   **Live embryo collection for imaging**

272   For embryo collection, lids on fly cages were exchanged one hour prior to imaging. After one

273   hour, embryos were collected from the lids using an inoculation loop. A 5mm diameter glass

274   cover slip (#64-0700, Warner Instruments) was prepared by immersion in a small amount of glue

275   (prepared by dissolving adhesive from about 1/5 of a roll of double-sided Scotch tape overnight

276   in heptane) and was left to dry for 5-10 minutes while collecting embryos. Collection was

277   performed on a dissection scope with trans-illumination. Embryos were bathed in Halocarbon oil

278   27 (Sigma) for staging and then selected between developmental stages 1 and 4. Selected

279   embryos were placed on a small square of paper towel, then de-chorionated in 100% bleach for 1

280   minute. Bleach was wicked off with a Kimwipe after one minute, then the square was washed

281   with a small amount of distilled water. Excess water was wicked off the square and the square

282   was dipped in a small water bath. Un-punctured embryos that floated to the top of the bath were

283   selected for imaging and placed on a small paper towel square to slightly dry. To prevent excess

284   desiccation embryos were immediately placed on the glass cover slip in rows and then immersed

285   in a drop of phosphate-buffered saline (PBS).

286   **Lattice Light-Sheet Microscopy**

287   Imaging was performed using a home built lattice light-sheet microscope (Figure 1-figure

288   supplement 1) following the design described by Chen et al. (B. C. Chen et al., 2014) and

289   detailed blueprints provided by the Betzig group at HHMI Janelia Research Campus. To perform

290   the single molecule experiments we added a detection module containing two EMCCDs (Andor

291   iXon Ultra) for dual color imaging. The EMCCDs provided a significant improvement in signal

292   to noise over the sCMOS (Hamamatsu Orca Flash V2.0) used in the original system and made it

293   possible to use lower excitation powers while maintaining single molecule sensitivity. In brief,

294   the output beam from each laser is expanded and collimated independently to a size of 2.5 mm.

295   The expanded beams for each laser are combined and input into an Acoustic Optical Tunable

296   Filter (AOTF) to allow for rapid switching between excitation wavelengths and adjustment of

297   power (Figure 1-figure supplement 1A). A pair of cylindrical lenses is then used to elongate and

298   collimate the output Gaussian beam to illuminate a stripe on a spatial light modulator (SLM).

299   The SLM is used to generate a coherent pattern of an array of 30 Bessel beams spaced such that

300   they coherently interfere to create a 2D optical lattice pattern with a maximum numerical

301   aperture (NA) of 0.6 and minimum NA of 0.505. A 500 mm lens is used to project the Fourier

302   transform of the SLM plane onto an annular mask, conjugate to the back pupil plane (BPP) of the

303   excitation objective, to spatially filter the pattern (Figure 1-figure supplement 1B). The BPP is

304   then projected first onto a galvo scanning mirror for z-scanning and then onto a second galvo

305   scanning mirror for x-dithering. The x-galvo scanning plane is projected onto the BPP of the

306   excitation objective (Figure 1-figure supplement 1C). The excitation objective focuses the lattice

307   pattern onto the sample, exciting any fluorophores within the axial range (~400nm) of the sheet.

308   The emitted fluorescence is collected by the detection objective which is oriented orthogonally to

309   the excitation objective and projected onto an intermediate image plane by a 500 mm tube lens

310   (Figure 1-figure supplement 1D). An 80 mm and 200 mm lens pair is then used to de-magnify

311   the image further to provide a 100 nm sampling per pixel on each of the EMCCD sensors. A

312   dichroic mirror (Semrock FF560-FDi01) is placed between the last lens pair to allow for dual

313   color imaging in red and green with maximal spectral separation. An emission filter is placed in

314   the path of each camera to both reject the excitation wavelengths and also select the wavelength

315   range of interest (Semrock FF03-525/50 for eGFP and FF01-593/46 for RFP) (Figure 1-figure

316   supplement 1E). During each camera exposure the x-galvo mirror is dithered twice over a 5.1 µm

317   range in 100 nm steps to provide uniform illumination.

318   The prepared coverslip, with embryos arranged in rows as described above, was then

319   loaded into the sample holder and secured on to the positioning stages of the lattice light-sheet

320   microscope. The sample chamber was filled with PBS for imaging and kept at room temperature.

321   The slide was then scanned to find an embryo of suitable age (between nuclear cycles 10 and11)

322   and the positions of the anterior and posterior extremes of the embryo were then marked. For

323   each dataset acquired, the stage position was recorded to determine the position as a fraction of

324   the embryonic length (EL) as the distance of the position from the anterior pole divided by the

325   total length of the embryo.

326   For the residence time measurements on BCD-eGFP, a 488 nm excitation laser was used

327   with a power of 2.9 mW measured at the back pupil plane of the excitation objective. Images

328   were acquired with 100 millisecond exposure times and an EM Gain setting of 300. At each

329   location at least 1000 frames were acquired resulting in a total time of 105 seconds, with a frame

330   rate of 105 ms. Prior to and after acquiring the BCD-eGFP data an image was taken in His2-

331   AVmRFP using a 561 nm excitation laser at an excitation power of ~0.17 mW at the back pupil

332   plan to determine the nuclear cycle phase, data not acquired during interphase was discarded

333   upon examination of these images. For residence time measurements at 500 ms exposure times,

334   the 488 nm excitation laser power at the back pupil plane was reduced to 0.5 mW all other

335   settings were the same as above. For the displacement distribution measurements the exposure

336   time was set to 10 ms, resulting in a frame rate of 15 ms and the excitation power was increased

337   to 8.28 mW for the 488 nm laser line. All other settings were the same as described above.

338   Viability of the embryos was determined by allowing them to develop till gastrulation after

339   imaging. For the *zelda-* embryos lethality was confirmed after imaging.

340   **Curation of data for analysis**

341   For all datasets the following procedure was followed: First, for each movie the corresponding

342   before-and-after histone images were checked for any evidence of chromatin condensation to

343   ensure that analysis was only performed in interphase nuclei. Data from mid-to-late nuclear cycle

344   14, where the nuclei exhibit an elongated shape, were also excluded. A metadata file was then

345   created for each movie file containing the position as a fraction of the embryonic length (0 for

346 anterior, 1 for posterior), the nuclear cycle (determined by counting the number of mitoses before

347 the 14th cycle). Visual examination of the dataset was used to determine if there was any motion

348 of the nuclei during the acquisition period. Movies that contained any detectable motion were

349 discarded or cropped to only include the time interval where there was no motion. A rectangular

350 region of interest was then drawn around each nucleus which was then used to crop areas around

351 individual nuclei. The boundary of each nucleus was then marked using a hand-drawn polygon.

352 A masked movie was then created for each nucleus where regions outside the nucleus were set to

353 0 gray scale values so that all the analyses described below were only performed on molecules

354 within nuclear regions.

355 **Single molecule localization and tracking using Dynamic Multiple-target tracing (MTT)**

356 Localization and tracking of single molecules was conducting using a MATLAB implementation

357 of the MTT algorithm (Serge, Bertaux, Rigneault, & Marguet, 2008). In brief, the algorithm first

358 performs a bi-dimension Gaussian fitting to localize particles constrained by a log-likelihood

359 ratio test subject to the localization error threshold. Deflation looping is performed to detect

360 molecules that are partially overlapping. The parameters of the localization and tracking

361 algorithms were empirically determined through iterative examination of the results. For all data

362 sets the following settings were used: For localization, maximum number of deflation loops was

363 set to 10, localization error to 10^{-6}. For tracking the maximum expected diffusion coefficient was

364 set to 5 μm^2/s, maximum number of competitors was set to 1, and maximum off/blinking-frames

365 was set to 1.

366 **Residence time analysis**

367   The residence times were estimated from the 100 millisecond data using the results from

368 the single particle tracking using the MTT algorithm. The data was pooled into bins

16

369   corresponding to the position along the A-P axis of the embryo in 1/3 fractions of the embryonic

370   length (EL, 0-1 anterior to posterior), with the following number of nuclei and single molecule

371   trajectories per position bin:

372   Anterior: 34 nuclei, 17735, trajectories

373   Middle: 70 nuclei, 40092 trajectories

374   Posterior: 83 nuclei; 20823 trajectories

375   In the ZLD- embryos we measured the following number of nuclei and single molecule

376   trajectories per position bin:

377   Anterior: 23 nuclei, 11415, trajectories

378   Middle: 31 nuclei, 7572 trajectories

379   Posterior: 31 nuclei; 3606 trajectories

380   The survival probability distribution was then calculated as 1- the cumulative distribution

381   function of the trajectory lengths and was fit to both single and double exponential

382   models(Mazza, Abernathy, Golob, Morisaki, & McNally, 2012). The double exponential model

383   fit the data better in all cases (Figure 1-figure supplement. 3 and 4). The model used to fit the

384   data and to calculate the time constants and fraction of the population is:

$$Surival \Pr obability\,(t) = A(F_a e^{-k_s t} + (1 - F_a)e^{-k_{ns}t})$$

386   Where k_s and k_{ns} are the low (specific) and high (non-specific) off-rates respectively. The total

387   pooled datasets of 78650 trajectories from the MTT results from 187 nuclei were also fit in the

388   same manner.

389   To correct for photo-bleaching we used a *His2Av-eGFP* to estimate the bleaching

390   constant (0.00426 s^{-1}) and correct the off-rate as $k_{s,corrected}=k_s-k_{bleach}$.(Table 1). We note that the

391   bleaching correction has minimal effect on our estimated off-rates. The fact that we are not

17

392 limited by bleaching due to the transient nature of BCD binding is further validated through even

393 longer, 500 milliseconds exposure time measurements on 17 nuclei which provides an estimate

394 for the specific and non-specific off-rates that do not differ significantly from those measured at

395 100 milliseconds (Figure 1-figure supplement 4 and Table 1). The results of the fits to all data

396 are shown in Table 1.

397 **<u>Fluorescence Recovery After Photobleaching (FRAP)</u>**

398 Experiments were performed on a Zeiss LSM 800 laser scanning confocal system

399 (coupled to a Zeiss Axio Observer Z1) using a Plan-Achromat 63x/1.4 NA Oil immersion

400 objective and GaAsP-PMT detector and a 488 nm laser. A circular bleach region with a diameter

401 of 1.5 µm was used and the bleach location was selected manually in each nucleus at

402 approximately the center and a total bleach time of 78.1 ms was used. Data was acquired for at

403 least 1 second prior to bleaching and for at least 6 seconds post bleaching, with a time interval of

404 0.430 ms. Experiments were performed using live embryos from the same fly-line as for lattice

405 light-sheet imaging and which were collected and prepared in the same manner as described

406 above with the exception of the mounting procedure. For FRAP the embryos were mounted

407 between a semipermeable membrane (Biofolie; In Vitro Systems & Services) and a coverslip and

408 then embedded in Halocarbon 27 oil (Sigma). As in the case of the single molecule

409 measurements, the embryos were staged using the HIS2-AV-MRFP channel and all data was

410 acquired on embryos in nuclear cycle 13. The data was acquired on 21 nuclei all within the first

411 25% of the embryonic length from the anterior pole. FRAP experiments could not be performed

412 at more anterior locations due to the low BCD concentrations and thus signal to noise ratio.

413 For analysis, the spatial and temporal location of the bleach region was retrieved from the

414 meta-data recorded by the microscope control software and manually verified by inspecting the

415   data. Due to the short duration of the movies and rapid recovery drift correction was not

416   necessary. Each nucleus was manually segmented from the rest of the image by defining a

417   polygon region of interest. A region of interest the same size as the bleach region was also

418   marked in an area of each image outside of the nuclear region to be used to measure the

419   background or dark intensity. The FRAP curve for each nucleus was then calculated as follows:

420   First, the mean intensity in the nuclear region, $I_{nuc}(t)$, bleach region, $I_{bleach}(t)$, and

421   background region $I_{dark}(t)$ regions were calculated at each frame.

422   The background intensity was them subtracted from both the mean nuclear and bleach

423   region intensities. To correct for photo-bleaching from imaging the bleach region intensity was

424   then divided by the mean nuclear intensity at each time point. The resulting photo-bleaching

425   corrected intensity was then normalized to the mean pre-bleach intensity, calculated as the

426   average intensity in all frames prior to bleaching ($I_{pre-bleach}$). The final FRAP curve for each

427   nucleus was thus calculated as:

428    $$FRAP(t)= [(I_{bleach}(t),-I_{dark}(t)/ (I_{nuc}(t)- I_{dark}(t))]/ I_{pre-bleach}$$

429   The calculated FRAP curves for each nucleus were then aligned to the bleach frame and

430   averaged to generate the average FRAP curve shown in Fig. 1D. The averaged recovery data was

431   then fit to both a single exponential (1-A*exp([-ka*t]) and double exponential (1-A*exp([-ka*t]-

432   B*exp([-kb*t]) model (Figure 1-figure supplement 5 A,B), to measure the recovery time

433   constants. There is no significant difference in the quality of fit between the two models. For

434   comparison, the exact same experimental and analysis procedure was followed for His2AV-

435   MRFP1 (Figure 1-figure supplement 5 C) in the same embryos with the exception of using a 561

436   nm bleach laser, 3 nuclei were measured with these settings. For the histone measurements the

19

437 two-exponent fit was significantly better than the one-exponent as expected (Figure 1-figure

438 supplement 5).

Displacement Distribution Analysis

440   Single molecule trajectories were analyzed as described above. A total of 158 nuclei from

441 4 embryos were analyzed. The data from nuclei were binned according to their position along the

442 A-P axis in 1/3 fractions of the embryonic length (EL, 0-1 anterior to posterior), with the

443 following number of nuclei and single molecule displacements per bin: In the anterior most (0-

444 0.2) positions, tracking could not be performed reliably due to the high concentrations of Bicoid

445 at those locations at these high frame rates and presumably a large mobile population.

446 Anterior: 30 nuclei, 12923, trajectories

447 Middle: 67 nuclei, 23640 trajectories

448 Posterior: 66 nuclei; 8600 trajectories

449   The fraction of the population that is bound vs. mobile was estimated using two

450 approaches. First, a cumulative distribution function of the displacements was calculated for each

451 EL bin (Figure 2-figure supplement 1A), displacements corresponding to distances less than a

452 value of 225 nm were scored as part of the bound population. In the second approach the

453 probability density functions of the displacements were fit to a two population model (Figure 2-

454 figure supplement 1B).

455 $$P(r) = F_{Bound} \frac{r}{A} e^{\frac{r^2}{2A}} + (1 - F_{Bound}) \frac{r}{B} e^{\frac{r^2}{2B}}$$

456   Where F_{Bound} is the fraction of the population that is considered bound and r is the

457 displacement distance. The two population model fits the displacement data with R^2 values of

458 0.97, 0.98, and 0.96, for the anterior, middle and posterior distributions respectively and provides

459 an estimate of the fraction present in the mobile and bound populations. The trend of an increase

20

460   in the population bound estimate in the middle and posterior positions relative to the anterior is

461   similar from both approaches. Although the bound population includes non-specific binding

462   events as well, what we are interested in the relative change across the A-P axis.

463   We note that the diffusion coefficients for the bound and mobile populations can in

464   principle be estimated from displacement distributions, however as explained by Mazza et al.

465   (Mazza et al., 2012):, they cannot be estimated accurately from a fit to a displacement

466   distribution at a single time step and are thus not reported. To accurately measure the diffusion

467   coefficients more stable and photo switchable fluorophores are necessary to be able to track

468   single molecules for more time points and at higher time resolutions.

469   **<u>DBSCAN based analyses of clusters</u>**

470   The clustering of Bicoid binding events in the 100 millisecond WT embryos dataset is

471   readily apparent in nuclei across the A-P axis in the projection of all localizations from the MTT

472   algorithm (Figure. 2B). In order to automatically identify clusters and count the number of

473   detections/ cluster vs. the whole nucleus (Figure. 2C), a MATLAB implementation (Yarpiz

474   Team 2015) of the widely used Density-based spatial clustering of applications with noise

475   (DBSCAN) was used with a minimum points setting of 10 points and an epsilon (maximum

476   radius of neighborhood) setting of 0.8. These settings were empirically determined by iteratively

477   changing parameters and examining the results. A balance had to be struck in an ability to

478   accurately identify clusters in the high density situations in anterior nuclei and also low density

479   situations in the posterior. Only datasets with timespans of at least 105 seconds were included. A

480   total of 12, 49, and 48 nuclei and 436, 1168, and 367 clusters were analyzed in this manner for

481   the Anterior, Middle, and Posterior positions respectively. Examples of clusters identified in

482   nuclei at various positions are shown in Figure 3-figure supplement 2. For comparing

483   distributions outliers were removed ($< 5^{th}$ or $> 95^{th}$ percentile) to disregard clusters that were

484   significantly over or under-partitioned. In the case of the ZLD- embryos, due to the loss of

485   apparent clustering, DBSCAN was not able to detect clusters so instead the spatial distribution of

486   points was compared using pair-correlation analysis as described below to provide insight on the

487   change beyond visual examination.

Pair correlation analysis of clustering

489   The pair correlation function for the spatial distribution of particles computes the probability of

490   finding a particle at the range of distances from another particles. In the case of complete spatial

491   randomness which can be represented by a Poisson process the pair correlation function is equal

492   to 1. The analysis is conducted on point lists generated from the MTT algorithm using the first

493   spatial coordinate of each trajectory. A total of 22, 48, and 42 nuclei were used for the Anterior,

494   Middle, and Posterior positions respectively for the WT embryos and a total of 23, 31, and 31

495   nuclei were used for the Anterior, Middle, and Posterior positions respectively for the *zld-*

496   embryos. A MATLAB implementation (Ilya Valmianski 2014) was used to calculate the

497   correlation function for the spatial distribution in each nucleus, the results were then averaged for

498   each position (Anterior, Middle, Posterior) embryo for comparison (Figure 3-figure supplement

499   3).

Chromatin Immunoprecipitation and Sequencing (ChIP-Seq)

501   Embryos were collected from a population cage for 90 minutes and then aged for 2 hours in

502   order to enrich for embryos at developmental stage five. Embryos were then fixed with

503   formaldehyde as previously described (Li et al., 2008) and sorted by morphology for those at

504   early stage 5. The posterior thirds of embryos were sliced off by hand with a scalpel. A pool of

505   the embryo segments from approximately 300 embryos was combined with 20 µg of whole

506　　*Drosophila pseudoobscura* embryos at stage 5 (to serve as carrier), and homogenized in

507　　homogenization buffer containing 15mM NaCl, 15mM TrisHCl pH 7.5, 60mM KCl, 1mM

508　　EDTA, and 0.1% Triton-X100, with 1mM DTT, 0.1 mM PMSF, and protease inhibit cocktail

509　　(Roche) added before use. After homogenization, 0.5% NP40 was added, and following a 5

510　　minute incubation, samples were spun down at a low speed. Nuclei in the pellet were then

511　　washed once with the homogenization buffer containing 0.2M NaCl. The low speed

512　　centrifugation was repeated, and the recovered nuclei pellet was then re-suspended in nuclear

513　　lysis buffer (10 mM TrisCl, pH 7.9, 100 mM NaCl, 1 mM EDTA, 0.5 % Sarkosyl) +1%SDS,

514　　+1.5% sarkosyl. The chromatin was recovered by spinning the sample at full speed in a micro-

515　　centrifuge at 4°C for 1 hour and was re-suspended in a small volume of nuclear lysis buffer.

516　　Chromatin was sheared to an average size of 300bp using a Covaris sonicator (peak power= 140,

517　　duty factor = wo, cycle burst = 200, time = 2:20 minutes). Chromatin immunoprecipitation was

518　　performed using 72ng of chromatin and 1.5ug of an anti-Bicoid polyclonal antibody described

519　　previously (Li et al., 2008). The Bicoid antibody was coupled to Dynabead M-280 sheep anti-

520　　rabbit magnetic beads and the immunoprecipitation was conducted with the standard protocol

521　　from the manufacturer. DNA libraries for the chromatin immunoprecitation samples were

522　　prepared using the Rubicon genomics thru-plex DNA-seq kit using 16 PCR cycles and

523　　sequenced using Illumina High-seq with 2500 rapid run100bp single end reads. The sequencing

524　　reads were aligned to a combined *D. pseudoobscura* (Flybase Release 1.0) and *D. melanogaster*

525　　genome (Flybase Release 5) using Bowtie with options set as -3 70 -n 2 -m 1. The aligned reads

526　　were converted to wig files using custom scripts available upon request. Wig files were

527　　normalized to 10 million mapped reads.

528　　**ChIP-Seq analysis**

529   The posterior embryo ChIP-seq data was compared to published data on whole embryos from the

530   same developmental stage (Bradley et al., 2010) downloaded from the NCBI GEO database with

531   accession number GSM511083. To compare against Zelda binding, previously published data

532   (Harrison et al., 2011) was downloaded from the NCBI GEO database with accession number

533   GSM763061. Since the purpose of the analysis was to compare relative enrichment at genomic

534   loci over each datasets respective background, the following normalization procedure was used:

535   First, for each chromosome the average of the signal over the entire chromosome (a proxy for the

536   background signal) was subtracted, negative values were then treated as below the background

537   and discarded. The data was then normalized to the background subtracted average of each

538   chromosome such that the normalized data now represents enrichment over background. For

539   visualization data was smoothed using a Savitzky-Golay filter of order 3 over a 0.250 kbp sliding

540   window. For analysis on CRMs the RedFly annotation database was used. For analysis centered

541   on called peaks in either the whole embryo BCD data or the Zelda data .bed files containing peak

542   locations were downloaded from the NCBI GEO database.

543   **ACKNOWLEDGMENTS**

555 **COMPETING INTERESTS**

556   We have no competing interests to declare.

557 **REFERENCES**

558 Bradley, R. K., Li, X. Y., Trapnell, C., Davidson, S., Pachter, L., Chu, H. C., . . . Eisen, M. B. (2010). Binding Site
559   Turnover Produces Pervasive Quantitative Changes in Transcription Factor Binding between Closely
560   Related Drosophila Species. *Plos Biology, 8*(3). doi: ARTN e1000343
561 10.1371/journal.pbio.1000343
562 Burz, D. S., Rivera-Pomar, R., Jackle, H., & Hanes, S. D. (1998). Cooperative DNA-binding by Bicoid provides a
563   mechanism for threshold-dependent gene activation in the Drosophila embryo. *EMBO J, 17*(20), 5998-
564   6009. doi: 10.1093/emboj/17.20.5998
565 Chen, B. C., Legant, W. R., Wang, K., Shao, L., Milkie, D. E., Davidson, M. W., . . . Betzig, E. (2014). Lattice light-
566   sheet microscopy: Imaging molecules to embryos at high spatiotemporal resolution. *Science, 346*(6208),
567   439-439. doi: DOI 10.1126/science.1257998
568 Chen, H., Xu, Z., Mei, C., Yu, D., & Small, S. (2012). A system of repressor gradients spatially organizes the
569   boundaries of Bicoid-dependent target genes. *Cell, 149*(3), 618-629. doi: 10.1016/j.cell.2012.03.018
570 Chen, J. J., Zhang, Z. J., Li, L., Chen, B. C., Revyakin, A., Hajj, B., . . . Liu, Z. (2014). Single-Molecule Dynamics
571   of Enhanceosome Assembly in Embryonic Stem Cells. *Cell, 156*(6), 1274-1285. doi: DOI
572   10.1016/j.cell.2014.01.062
573 Cisse, II, Izeddin, I., Causse, S. Z., Boudarene, L., Senecal, A., Muresan, L., . . . Darzacq, X. (2013). Real-time
574   dynamics of RNA polymerase II clustering in live human cells. *Science, 341*(6146), 664-667. doi:
575   10.1126/science.1239053
576 Combs, P., & Eisen, M. (2017). *Genome-wide measurement of spatial expression in patterning mutants of*
577   *Drosophila melanogaster [version 1; referees: 2 approved]* (Vol. 6).
578 Combs, P. A., & Eisen, M. B. (2013). Sequencing mRNA from Cryo-Sliced Drosophila Embryos to Determine
579   Genome-Wide Spatial Patterns of Gene Expression. *PLoS One, 8*(8). doi: ARTN e71820
580 10.1371/journal.pone.0071820
581 Crocker, J., Noon, E. P., & Stern, D. L. (2016). The Soft Touch: Low-Affinity Transcription Factor Binding Sites in
582   Development and Evolution. *Curr Top Dev Biol, 117*, 455-469. doi: 10.1016/bs.ctdb.2015.11.018
583 Crocker, J., Tsai, A., Muthusamy, A. K., Lavis, L. D., Singer, R. H., & Stern, D. L. (2017). Nuclear
584   Microenvironments Modulate Transcription From Low-Affinity Enhancers. *bioRxiv*. doi: 10.1101/128280
585 Driever, W., & Nusslein-Volhard, C. (1988a). The bicoid protein determines position in the Drosophila embryo in a
586   concentration-dependent manner. *Cell, 54*(1), 95-104.
587 Driever, W., & Nusslein-Volhard, C. (1988b). A gradient of bicoid protein in Drosophila embryos. *Cell, 54*(1), 83-
588   93.
589 Driever, W., & Nussleinvolhard, C. (1989). The Bicoid Protein Is a Positive Regulator of Hunchback Transcription
590   in the Early Drosophila Embryo. *Nature, 337*(6203), 138-143. doi: Doi 10.1038/337138a0
591 Driever, W., Siegel, V., & Nusslein-Volhard, C. (1990). Autonomous determination of anterior structures in the
592   early Drosophila embryo by the bicoid morphogen. *Development, 109*(4), 811-820.
593 Ephrussi, A., & St Johnston, D. (2004). Seeing is believing: the bicoid morphogen gradient matures. *Cell, 116*(2),
594   143-152.
595 Foo, S. M., Sun, Y., Lim, B., Ziukaite, R., O'Brien, K., Nien, C. Y., . . . Rushlow, C. A. (2014). Zelda potentiates
596   morphogen activity by increasing chromatin accessibility. *Current Biology, 24*(12), 1341-1346. doi:
597   10.1016/j.cub.2014.04.032

598 Gregor, T., Wieschaus, E. F., McGregor, A. P., Bialek, W., & Tank, D. W. (2007). Stability and nuclear dynamics of
599   the bicoid morphogen gradient. *Cell, 130*(1), 141-152. doi: 10.1016/j.cell.2007.05.026
600 Hamm, D. C., Bondra, E. R., & Harrison, M. M. (2015). Transcriptional activation is a conserved feature of the
601   early embryonic factor Zelda that requires a cluster of four zinc fingers for DNA binding and a low-
602   complexity activation domain. *Journal of Biological Chemistry, 290*(6), 3508-3518. doi:
603   10.1074/jbc.M114.602292
604 Hannon, C. E., Blythe, S. A., & Wieschaus, E. F. (2017). Concentration Dependent Chromatin States Induced by the
605   Bicoid Morphogen Gradient. *bioRxiv*. doi: 10.1101/133348
606 Hansen, A. S., Pustova, I., Cattoglio, C., Tjian, R., & Darzacq, X. (2017). CTCF and cohesin regulate chromatin
607   loop stability with distinct dynamics. *Elife, 6*, e25776. doi: 10.7554/eLife.25776
608 Harrison, M. M., Li, X. Y., Kaplan, T., Botchan, M. R., & Eisen, M. B. (2011). Zelda binding in the early
609   Drosophila melanogaster embryo marks regions subsequently activated at the maternal-to-zygotic
610   transition. *PLoS Genet, 7*(10), e1002266. doi: 10.1371/journal.pgen.1002266
611 La Rosee, A., Hader, T., Taubert, H., Rivera-Pomar, R., & Jackle, H. (1997). Mechanism and Bicoid-dependent
612   control of hairy stripe 7 expression in the posterior region of the Drosophila embryo. *EMBO J, 16*(14),
613   4403-4411. doi: 10.1093/emboj/16.14.4403
614 Lebrecht, D., Foehr, M., Smith, E., Lopes, F. J. P., Vanario-Alonso, C. E., Reinitz, J., . . . Hanes, S. D. (2005).
615   Bicoid cooperative DNA binding is critical for embryonic patterning in Drosophila. *Proceedings of the
616   National Academy of Sciences of the United States of America, 102*(37), 13176-13181. doi:
617   10.1073/pnas.0506462102
618 Li, X. Y., Harrison, M. M., Villata, J. E., Kaplan, T., & Eisen, M. B. (2014). Establishment of regions of genomic
619   activity during the Drosophila maternal to zygotic transition. *Elife, 3*. doi: ARTN e03737
620 10.7554/eLife.03737
621 Li, X. Y., MacArthur, S., Bourgon, R., Nix, D., Pollard, D. A., Iyer, V. N., . . . Biggin, M. D. (2008). Transcription
622   factors bind thousands of active and inactive regions in the Drosophila blastoderm. *Plos Biology, 6*(2), 365-
623   388. doi: ARTN e27
624 10.1371/journal.pbio.0060027
625 Liang, H. L., Nien, C. Y., Liu, H. Y., Metzstein, M. M., Kirov, N., & Rushlow, C. (2008). The zinc-finger protein
626   Zelda is a key activator of the early zygotic genome in Drosophila. *Nature, 456*(7220), 400-U467. doi:
627   10.1038/nature07388
628 Liu, Z., Lavis, L. D., & Betzig, E. (2015). Imaging Live-Cell Dynamics and Structure at the Single-Molecule Level.
629   *Mol Cell, 58*(4), 644-659. doi: 10.1016/j.molcel.2015.02.033
630 Liu, Z., Legant, W. R., Chen, B. C., Li, L., Grimm, J. B., Lavis, L. D., . . . Tjian, R. (2014). 3D imaging of Sox2
631   enhancer clusters in embryonic stem cells. *Elife, 3*. doi: ARTN e04236
632 DOI 10.7554/eLife.04236.001
633 Lucchetta, E. M., Lee, J. H., Fu, L. A., Patel, N. H., & Ismagilov, R. F. (2005). Dynamics of Drosophila embryonic
634   patterning network perturbed in space and time using microfluidics. *Nature, 434*(7037), 1134-1138. doi:
635   10.1038/nature03509
636 Mazza, D., Abernathy, A., Golob, N., Morisaki, T., & McNally, J. G. (2012). A benchmark for chromatin binding
637   measurements in live cells. *Nucleic Acids Res, 40*(15), e119. doi: 10.1093/nar/gks701
638 Morrison, A. H., Scheeler, M., Dubuis, J., & Gregor, T. (2012). Quantifying the Bicoid morphogen gradient in
639   living fly embryos. *Cold Spring Harb Protoc, 2012*(4), 398-406. doi: 10.1101/pdb.top068536
640 Normanno, D., Boudarene, L., Dugast-Darzacq, C., Chen, J., Richter, C., Proux, F., . . . Dahan, M. (2015). Probing
641   the target search of DNA-binding proteins in mammalian cells using TetR as model searcher. *Nat Commun,
642   6*, 7357. doi: 10.1038/ncomms8357
643 Ochoa-Espinosa, A., Yu, D. Y., Tsirigos, A., Struffi, P., & Small, S. (2009). Anterior-posterior positional
644   information in the absence of a strong Bicoid gradient. *Proceedings of the National Academy of Sciences of
645   the United States of America, 106*(10), 3823-3828. doi: 10.1073/pnas.0807878105
646 Ochoa-Espinosa, A., Yucel, G., Kaplan, L., Pare, A., Pura, N., Oberstein, A., . . . Small, S. (2005). The role of
647   binding site cluster strength in Bicoid-dependent patterning in Drosophila. *Proceedings of the National
648   Academy of Sciences of the United States of America, 102*(14), 4960-4965. doi: 10.1073/pnas.0500373102
649 Perry, M. W., Bothma, J. P., Luu, R. D., & Levine, M. (2012). Precision of hunchback expression in the Drosophila
650   embryo. *Current Biology, 22*(23), 2247-2252. doi: 10.1016/j.cub.2012.09.051
651 Porcher, A., Abu-Arish, A., Huart, S., Roelens, B., Fradin, C., & Dostatni, N. (2010). The time to measure positional
652   information: maternal Hunchback is required for the synchrony of the Bicoid transcriptional response at the
653   onset of zygotic transcription. *Development, 137*(16), 2795-2804. doi: 10.1242/dev.051300

654 Rivera-Pomar, R., Lu, X., Perrimon, N., Taubert, H., & Jackle, H. (1995). Activation of posterior gap gene
655   expression in the Drosophila blastoderm. *Nature, 376*(6537), 253-256. doi: 10.1038/376253a0
656 Schulz, K. N., Bondra, E. R., Moshe, A., Villalta, J. E., Lieb, J. D., Kaplan, T., . . . Harrison, M. M. (2015). Zelda is
657   differentially required for chromatin accessibility, transcription factor binding, and gene expression in the
658   early Drosophila embryo. *Genome Research, 25*(11), 1715-1726. doi: 10.1101/gr.192682.115
659 Serge, A., Bertaux, N., Rigneault, H., & Marguet, D. (2008). Dynamic multiple-target tracing to probe
660   spatiotemporal cartography of cell membranes. *Nat Methods, 5*(8), 687-694. doi: 10.1038/nmeth.1233
661 Small, S., Blair, A., & Levine, M. (1996). Regulation of two pair-rule stripes by a single enhancer in the Drosophila
662   embryo. *Developmental Biology, 175*(2), 314-324. doi: DOI 10.1006/dbio.1996.0117
663 Struhl, G., Struhl, K., & Macdonald, P. M. (1989). The Gradient Morphogen Bicoid Is a Concentration-Dependent
664   Transcriptional Activator. *Cell, 57*(7), 1259-1273. doi: Doi 10.1016/0092-8674(89)90062-7
665 Sun, Y. J., Nien, C. Y., Chen, K., Liu, H. Y., Johnston, J., Zeitlinger, J., & Rushlow, C. (2015). Zelda overcomes the
666   high intrinsic nucleosome barrier at enhancers during Drosophila zygotic genome activation. *Genome
667   Research, 25*(11), 1703-1714. doi: 10.1101/gr.192542.115
668 Tokunaga, M., Imamoto, N., & Sakata-Sogawa, K. (2008). Highly inclined thin illumination enables clear single-
669   molecule imaging in cells. *Nature Methods, 5*(2), 159-161. doi: 10.1038/Nmeth.1171
670 Turing, A. M. (1952). The Chemical Basis of Morphogenesis. *Philosophical Transactions of the Royal Society of
671   London Series B-Biological Sciences, 237*(641), 37-72. doi: DOI 10.1098/rstb.1952.0012
672 Wolpert, L. (1969). Positional Information and Pattern of Cellular Differentiation. *Biophysical Journal, 9*, A8-&.
673 Xu, H., Sepulveda, L. A., Figard, L., Sokac, A. M., & Golding, I. (2015). Combining protein and mRNA
674   quantification to decipher transcriptional regulation. *Nat Methods, 12*(8), 739-742. doi:
675   10.1038/nmeth.3446
676 Xu, Z., Chen, H., Ling, J., Yu, D., Struffi, P., & Small, S. (2014). Impacts of the ubiquitous factor Zelda on Bicoid-
677   dependent DNA binding and transcription in Drosophila. *Genes Dev, 28*(6), 608-621. doi:
678   10.1101/gad.234534.113

679

680

681

682
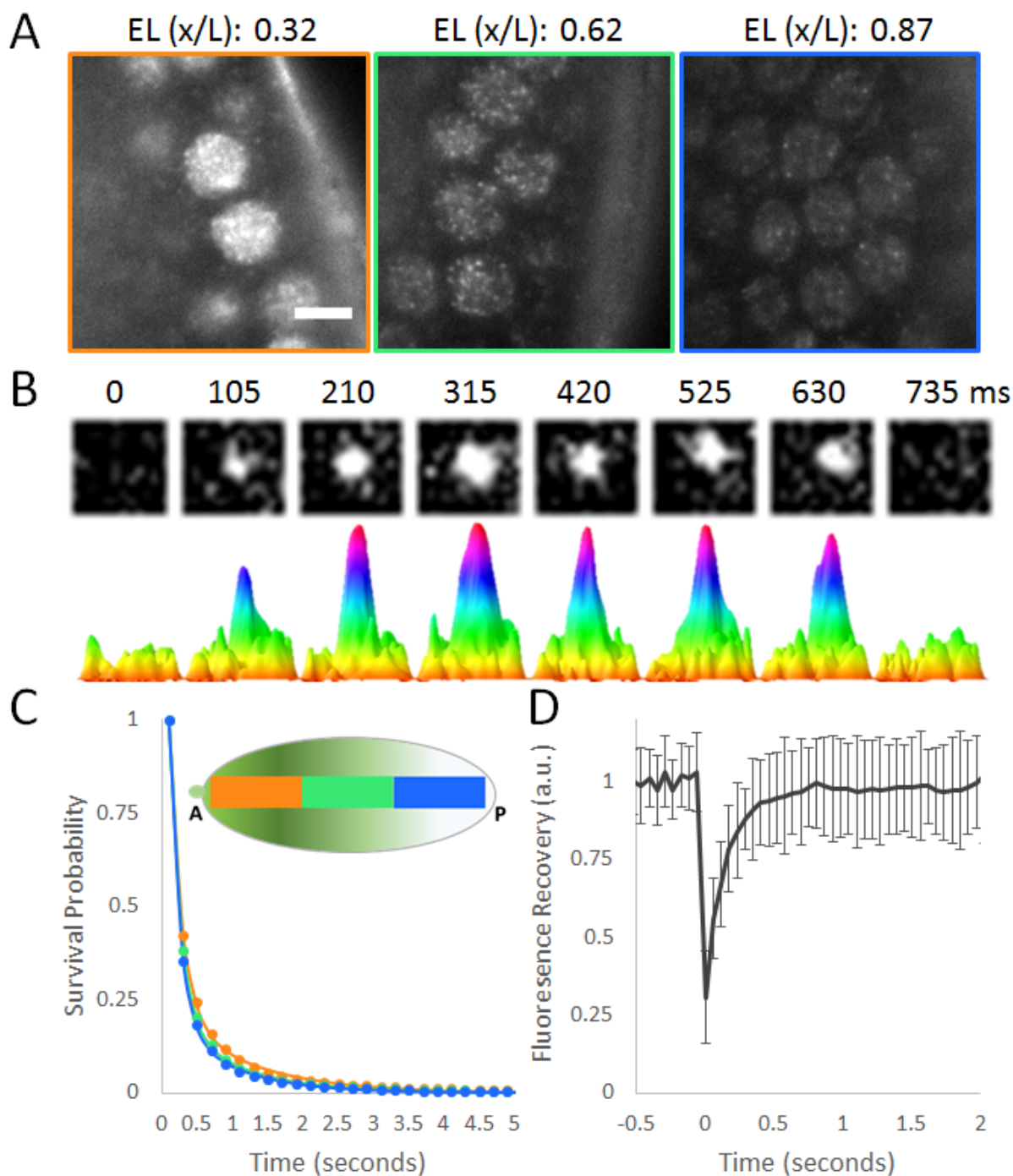
Figure. 1. Single molecule kinetics of Bicoid in living *Drosophila* Embryos. **(A)** Raw images of BCD-eGFP molecules in a living *Drosophila* embryo acquired with a 100 millisecond exposure time. Scale bar is 5 um. Positions along the A-P axis are shown as a fraction of the

686   Embryonic Length (EL, x/L). **(B)** Example of a single molecule binding event. Top row shows

687   raw images from a 1.2 x 1.2 µm area, bottom row shows corresponding surface plot

688   representations to illustrate the signal-to-noise. **(C)** Uncorrected survival probability curves for

689   Bicoid binding (markers) in the Anterior (34 nuclei), Middle (70 nuclei) and Posterior (83

690   nuclei) segments of the embryo and corresponding fits to a two-exponent model (solid lines)

691   show no significant differences. **(D)** FRAP curve for Bicoid shows a recovery time on the order

692   of hundreds of milliseconds, error bars show standard deviation over 21 nuclei.

693

Data Set	A-P Poistion	Non-specific binding time ($1/k_{ns}$ (sec))	Specific Binding time ($1/k_s$ (sec))	Corrected Specific Binding time $1/(k_s - k_{bleach})$ (sec)	Number of trajectories
100 ms	Ant	0.175 [0.166, 0.184]	1.100 [1.013, 1.203]	1.105	17735
	Mid	0.160 [0.152, 0.168]	0.940 [0.859, 1.038]	0.944	40092
	Post	0.146 [0.141, 0.151]	0.865 [0.806, 0.932]	0.868	20823
	All Together	0.159 [0.166, 0.152]	0.959 [0.882, 1.050]	0.963	78650
100 ms (Zelda-)	Ant	0.152 [0.146, 0.160]	0.777 [0.726, 0.836]	0.780	11415
	Mid	0.131 [0.126, 0.137]	0.629 [0.587, 0.679]	0.631	7572
	Post	0.112 [0.108, 0.117]	0.463 [0.435, 0.495]	0.464	3606
	All Together	0.139 [0.133, 0.145]	0.694 [0.647, 0.748]	0.696	22593
500 ms	All Together	0.265 [0.255, 0.277]	1.876 [1.69, 2.107]	-	1211

694

695 **Table 1. Results from 2-exponent model fits to survival probability distributions.**

696 k_{ns} and k_s are the un-corrected off-rates for the short-lived (non-specific) and longer-lived

697 (specific) populations respectively determined from a two-exponent fits to the survival

698 probability distributions. The binding time (one-over the off rates) are shown with 95%

699 confidence intervals in square brackets. The photo-bleaching corrected binding times are

700 calculated as $1/(k_s - k_{bleach})$ where k_{bleach} is 0.0043 s^{-1}).

701
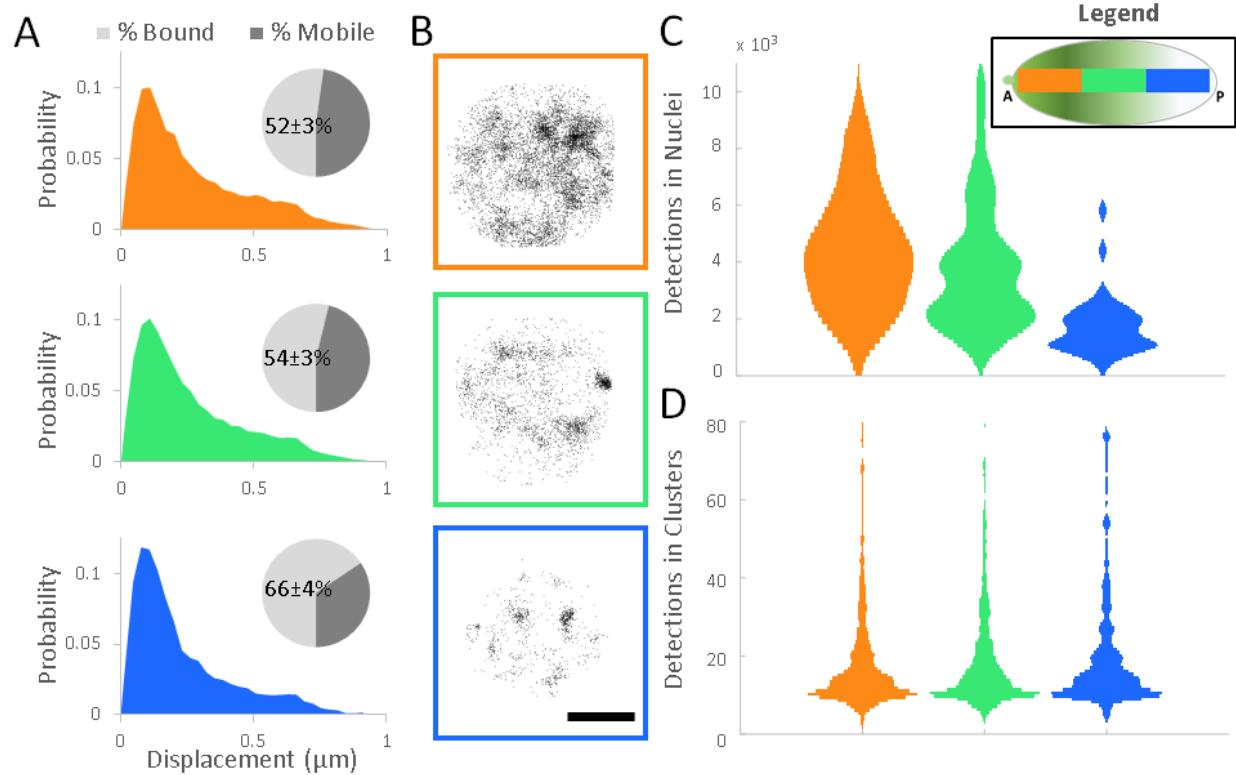
Figure. 2. Local modulation of Bicoid Concentration (A) Normalized probability distributions of measured displacements in the Anterior (30 nuclei), Middle (67 nuclei), and Posterior (66 nuclei) positions of the embryos, pie charts show the estimated mobile and bound fractions from fits to a two population distribution with the bound population percent labelled with the standard error of the fit parameter. **(B)** Examples of the spatial distribution of all detections in nuclei along the A-P axis, scale bar is 2.5 µm. **(C)** Distribution of the number of detections in all nuclei. **(D)** Distributions of the number of detections within all clusters.
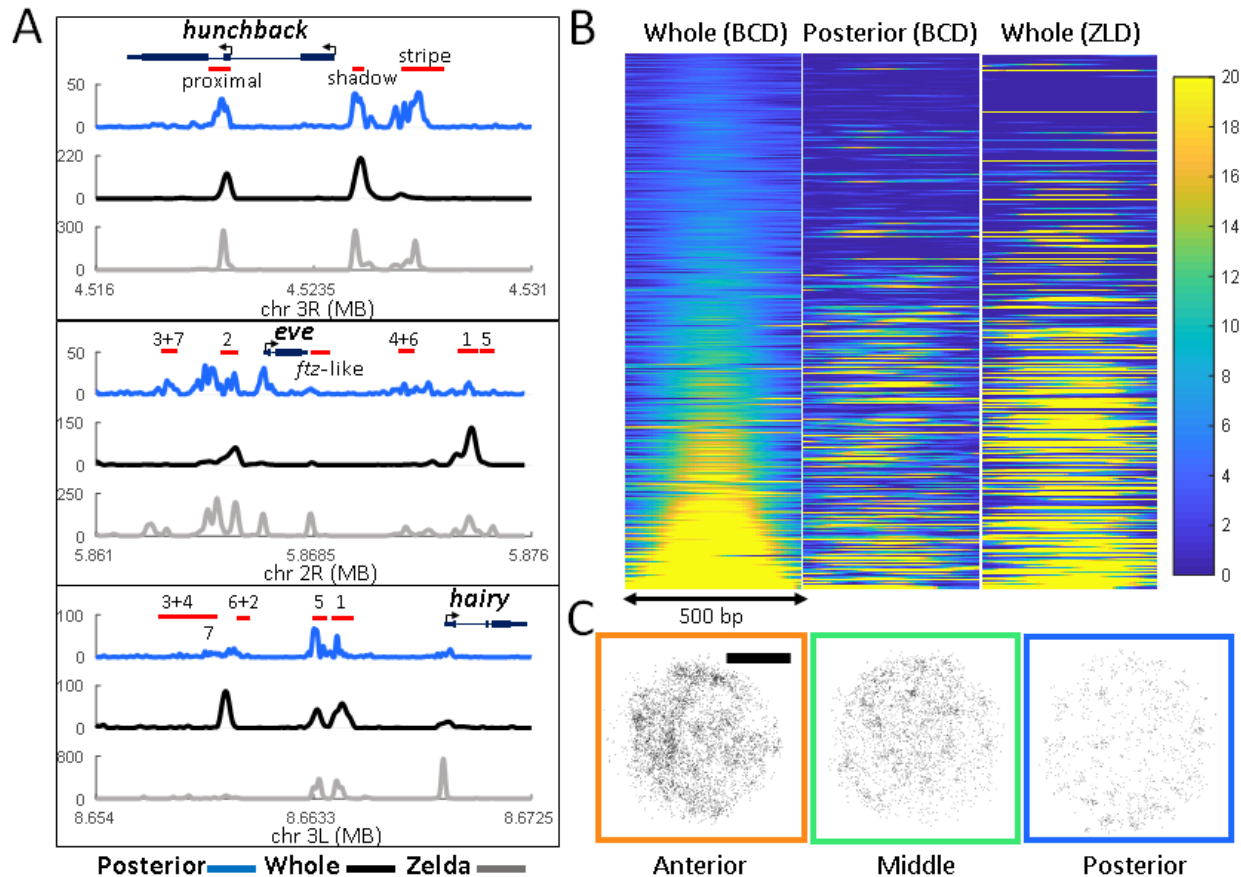
Figure. 3. Zelda mediated Bicoid binding in the posterior embryo (A) Posterior third (blue) and whole embryo (black) BCD, and whole embryo Zelda (grey) ChIP-seq signal normalized reads at the *hunchback*, *eve*, and *hairy* gene loci. Red bars show known enhancers as annotated in the RedFly database, for eve and hairy they are numbered according to the stripes they are thought to regulate. **(B)** Heat-map representation of normalized BCD ChIP-seq reads (first two panels) and ZLD-ChIP-seq reads (third panel) in a 500 bp window centered on BCD peaks called in the whole embryo data and sorted according to increasing signal of the whole embryo data, a total of 2145 peaks are shown, colors indicate enrichment over the background (blue) with all plots displayed on the same scale. **(C)** Examples of the spatial distribution of all detected bound molecules in nuclei along the A-P axis in ZLD- embryos, scale bar is 2.5 µm. A loss of clustering is apparent compared to the distributions shown in Figure 2B.

32

723

33

724
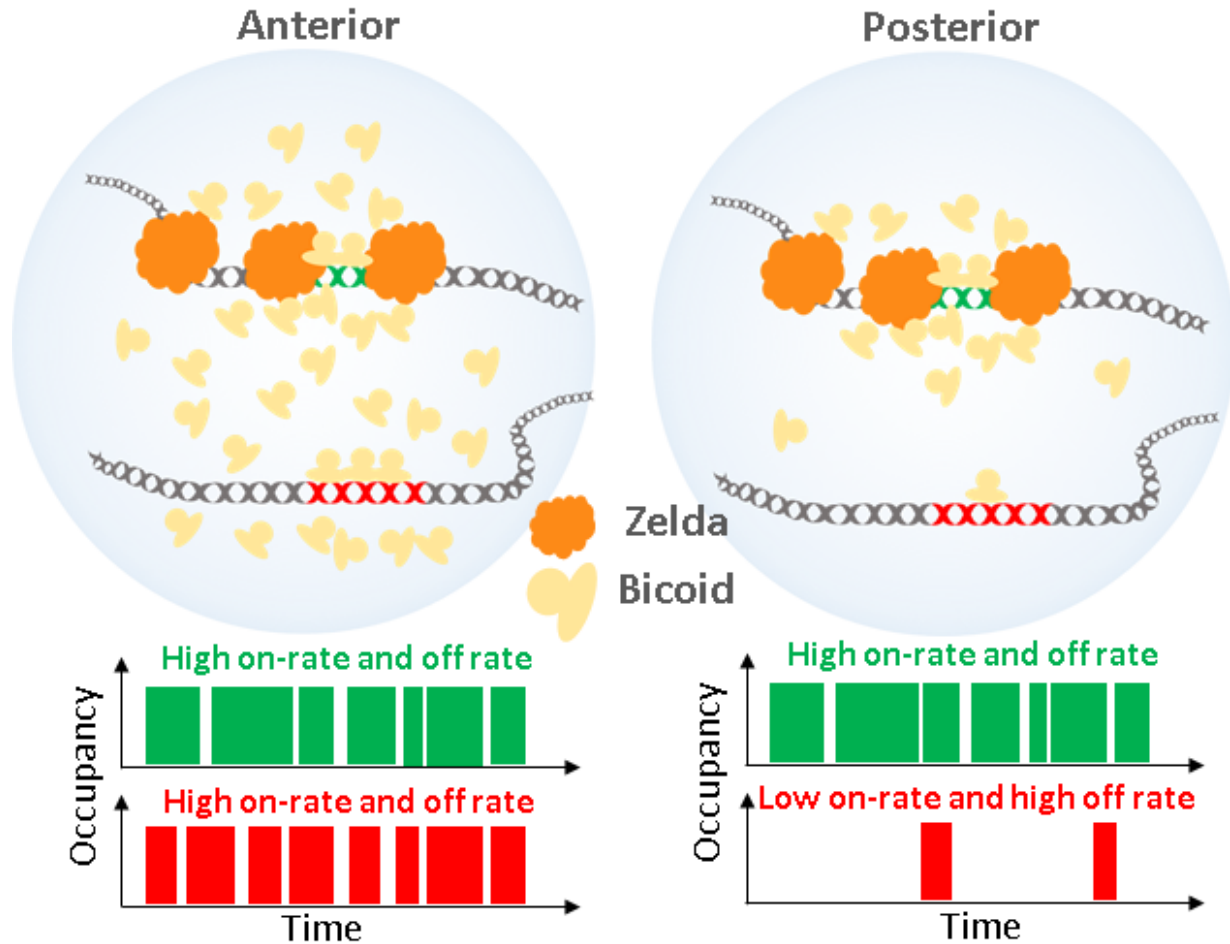
Figure. 4. Model of Zelda dependent modulation of the Bicoid on-rate at specific loci in the posterior embryo. At high concentrations in the anterior of the embryo, all target sites are highly occupied. At low concentrations, loci with Zelda occupancy have an increased time averaged occupancy through the formation of spatiotemporal hubs that enrich local concentrations and increase the on-rate.

730

731
732
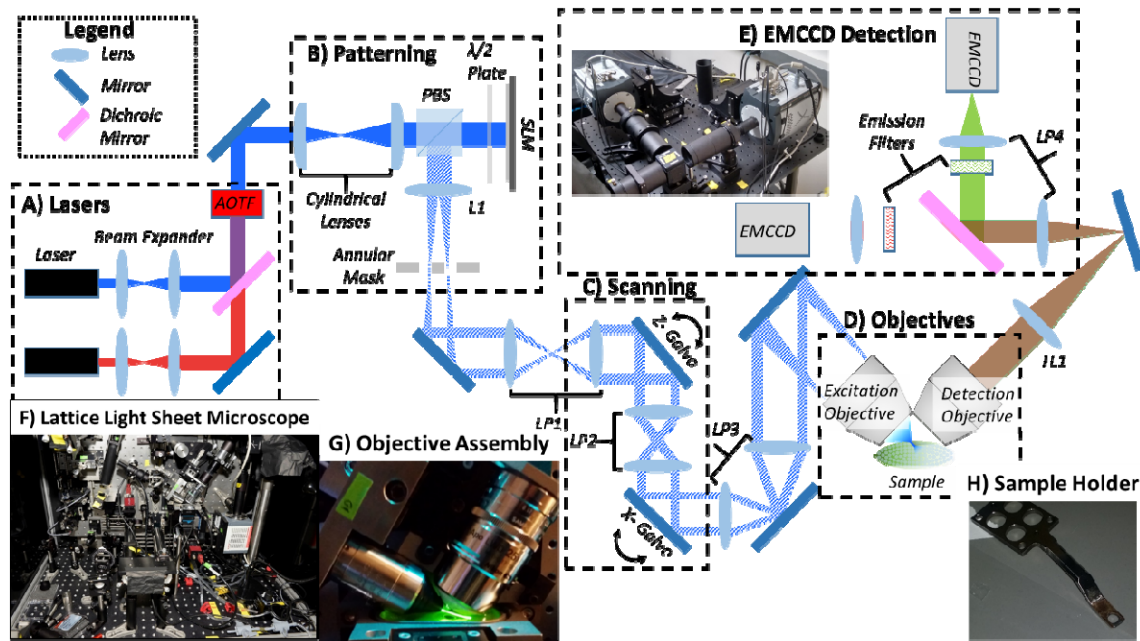
Figure1-figure supplement 1. Lattice Light-Sheet Microscope Implementation

The Lattice light-sheet was built as described by Chen et al, Science, 2014. This simplified schematic shows the major modules of the microscope as follows: **(A)** Laser Module, contains 6 lasers ranging from 405 nm to 639 nm, which are independently expanded, collimated, and input into an Acousto-Optic Tunable Filter (AOTF). **(B)** The patterning module contains a pair of cylindrical lens to expand the input Gaussian beam to a stripe, and a half-wave ($\lambda/2$) plate, a polarizing beam splitter (PBS), and a Spatial Light Modulator (SLM) to perform the patterning. Lens L1 projects the Fourier Transform of the SLM pattern onto an annular mask for spatial filtering **(C)** Lens pair 1 (LP1) is then used to de-magnify the annular mask plane and project it onto the z-scan galvo and LP2 projects the z-galvo plane onto the x-scanning galvo. **(D)** LP3 magnifies the x-galvo plane and projects it onto the back pupil plane of the excitation objective, where it is focused (Fourier transform) to project the final light sheet pattern onto the sample. Emitted fluorescence is collected by the detection objective. **(E)** The tube lens (TL1) focuses an intermediate image plane which is then magnified using LP4 and projected onto an EMCCD. A

35

747   dichroic mirror is placed between the first and second lenses of LP4 to split the signal into high

748   and low wavelengths. An emission filter is placed after the dichroic on both sides to select the

749   chromatic bandwidth of the signal reaching each EMMCD independently. Inset shows an image

750   of the EMCCD detection module (**F**) Image of our lattice light sheet microscope. (**G**) Image of

751   the Objective assembly with a dye solution in the sample chamber to visualize the excitation

752   light. (**H**) Image of the sample holder on which the 5 mm coverslip is mounted.

753
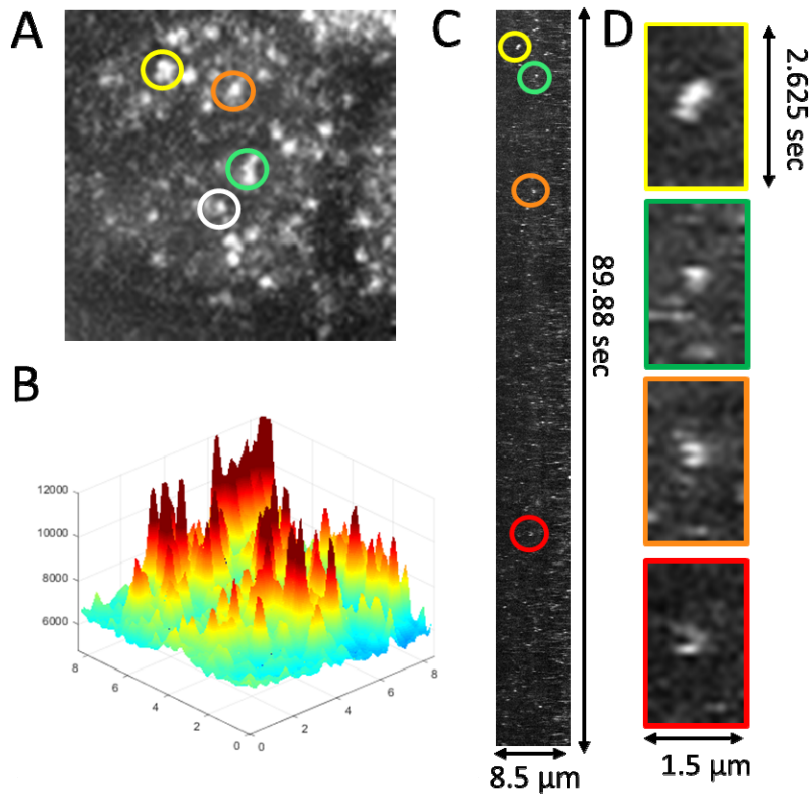
754
755 **Figure 1-figure supplement 2. Single Molecule Imaging of BCD-eGFP at 100 milliseconds**

756 **to estimate residence times**. **(A)** The max projection in time of a 90 second segment of a

757 representative 100 millisecond dataset acquired at an anterior nucleus (EL (x/L) of 0.1),

758 corresponding to the last frame of Video 2. **(B)** Surface plot representation of (A) to illustrate the

759 signal-to-background ratio of single molecule binding events. The smaller peaks likely

760 correspond to slowly diffusing molecules that are not in the imaging volume for the entire

761 exposure time. **(C)** Maximum projection through x-t (kymograph representation) of the data

762 shown in Video 2 from which (A-B) were calculated. Colored circles correspond to those in (A).

763 **(D)** Zoomed in x-t view of the circled regions in (A) and (C), illustrating the transient nature of

764 BCD binding.

765
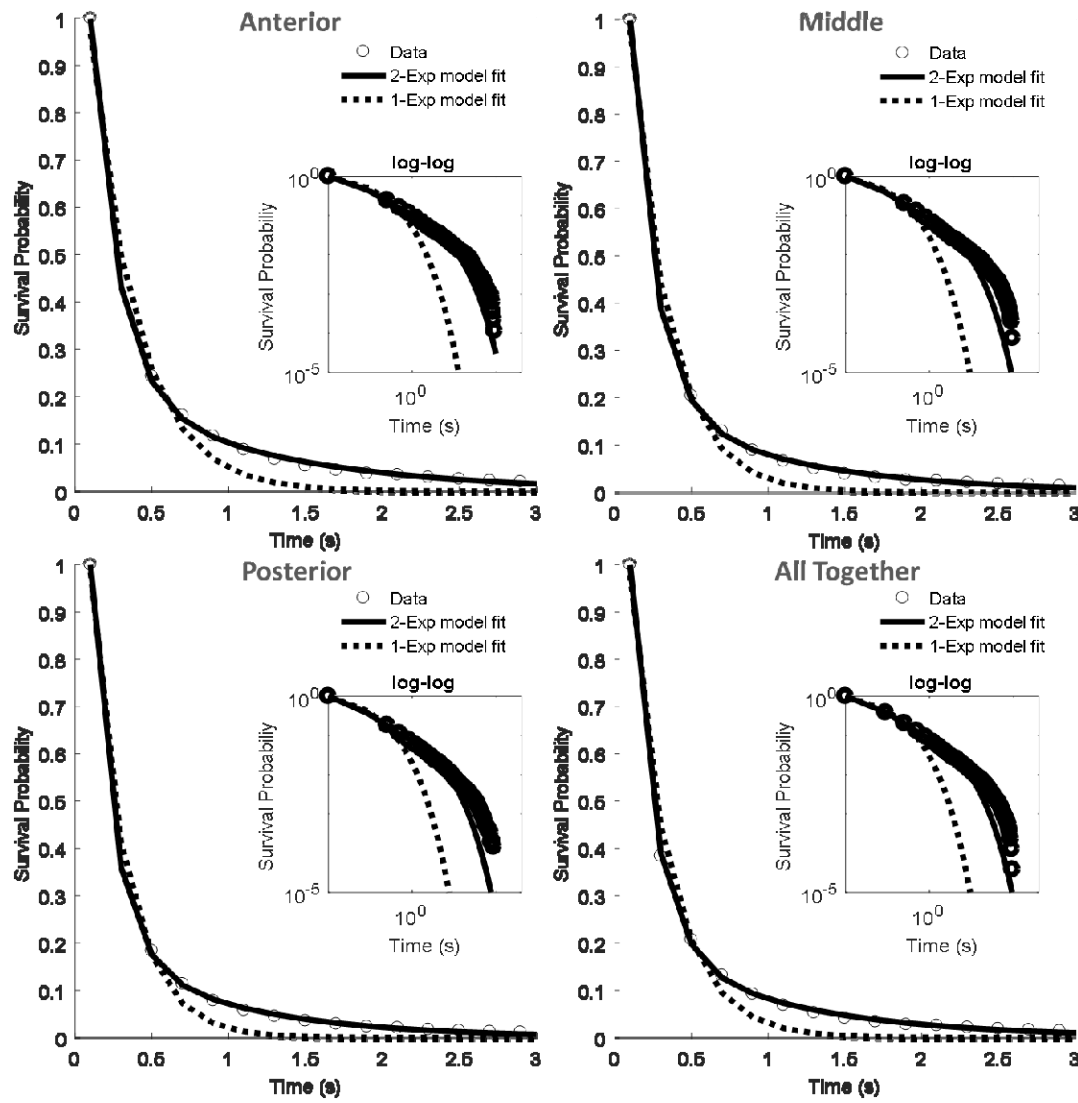
37

Figure 1-figure supplement 3. Fits to the survival probability distributions of the 100 millisecond datasets. The survival probability distributions calculated from the trajectories output by the MTT analysis on the 100 millisecond data set for the Anterior (34 nuclei, 17735, trajectories), Middle (70 nuclei, 40092 trajectories), Posterior (83 nuclei; 20823 trajectories) segments and all the data pooled together (187 nuclei, 78650 trajectories). The solid lines show the fit to a 2 exponent-model and the dashed lines to a 1-exponent model. Insets show the same

773   on a log-log scale to visualize the difference between 1 and 2 exponent fits at longer time scales.

774   All two-exponent fits have an R^2 value>0.99. See Table 1 for a summary of the fit parameters.

775
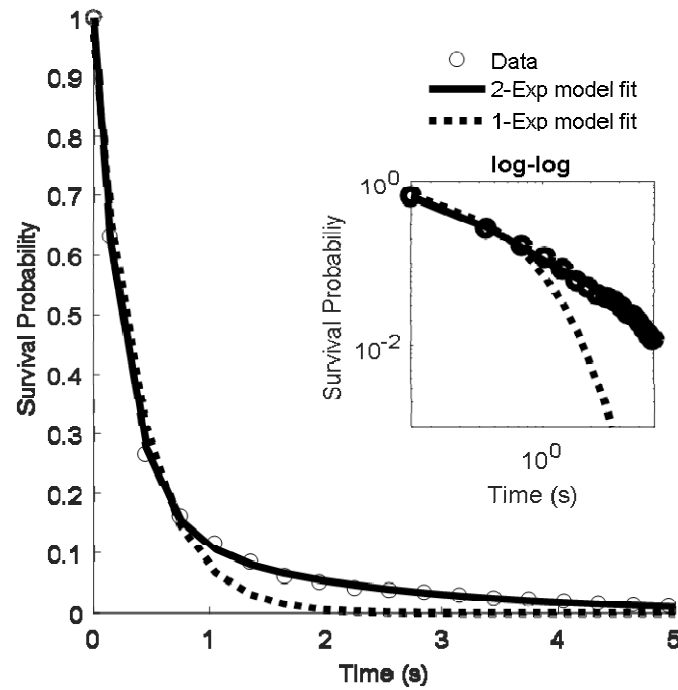
Figure 1- figure supplement 4. Fits to the survival probability distribution of the 500 millisecond dataset. The survival probability distribution of residence times calculated from the MTT algorithm on the 500 ms data set of 17 nuclei and 1211 trajectories. The solid lines show the fit to a 2-exponent model and the dotted lines to a 1-exponent model. The insets shows the same on a log-log scale to visualize the difference between 1 and 2 exponent fits. R^2 value for the 2-exponent fit is 0.99

785
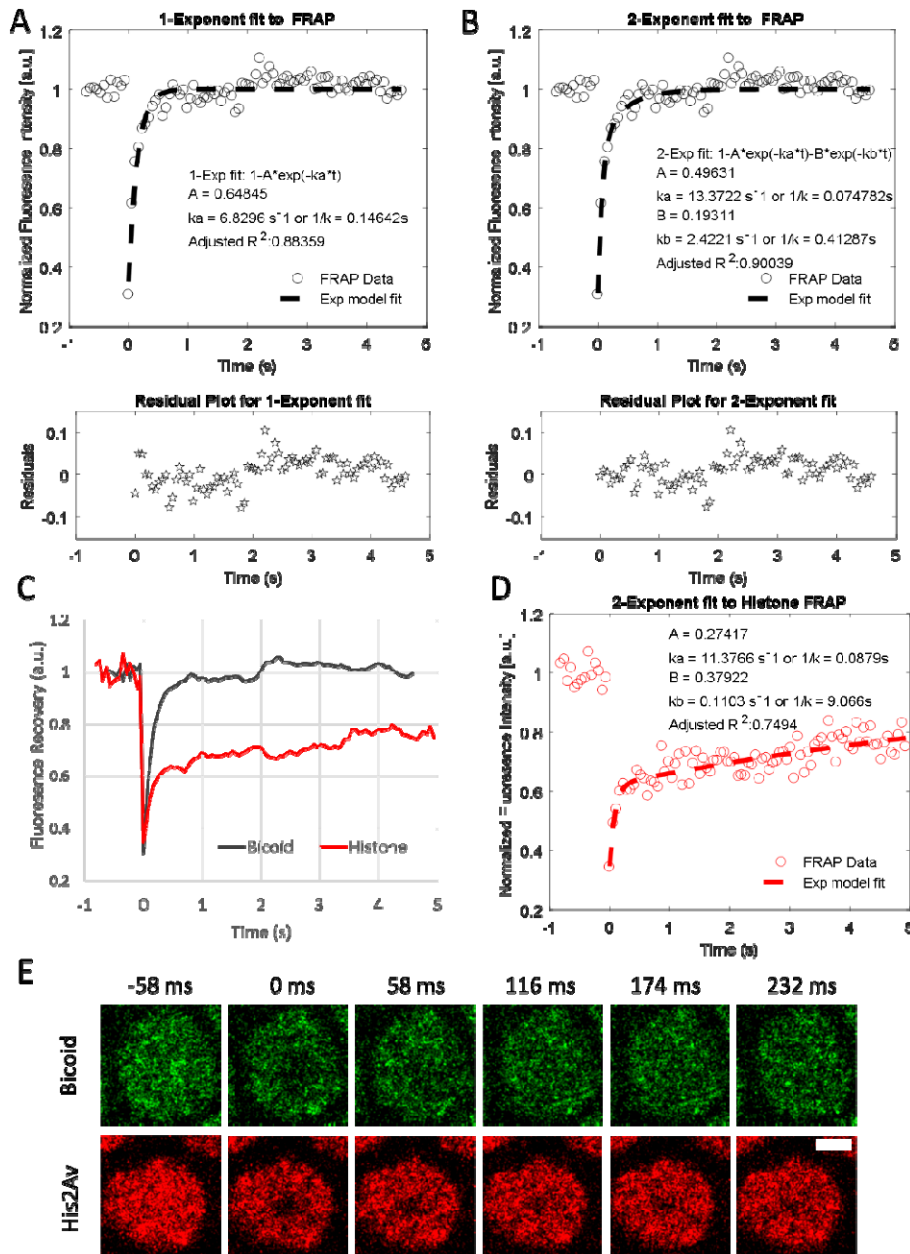
Figure 1- figure supplement 5. Analysis of FRAP data

(**A**) Averaged Bcd-eGFP FRAP data and single exponential fit results**. (B)** Double exponential fit results to average Bcd-eGFP FRAP**. (C)** Comparison of averaged BCD-eGFP (21 nuclei) and His2AV FRAP data (3 nuclei). (**D**) Double exponential fit to Histone (His2AV) FRAP. (**E**) Representative images from BCD-eGFP and His2AV FRAP experiments, white scale bar is 2µm.

792
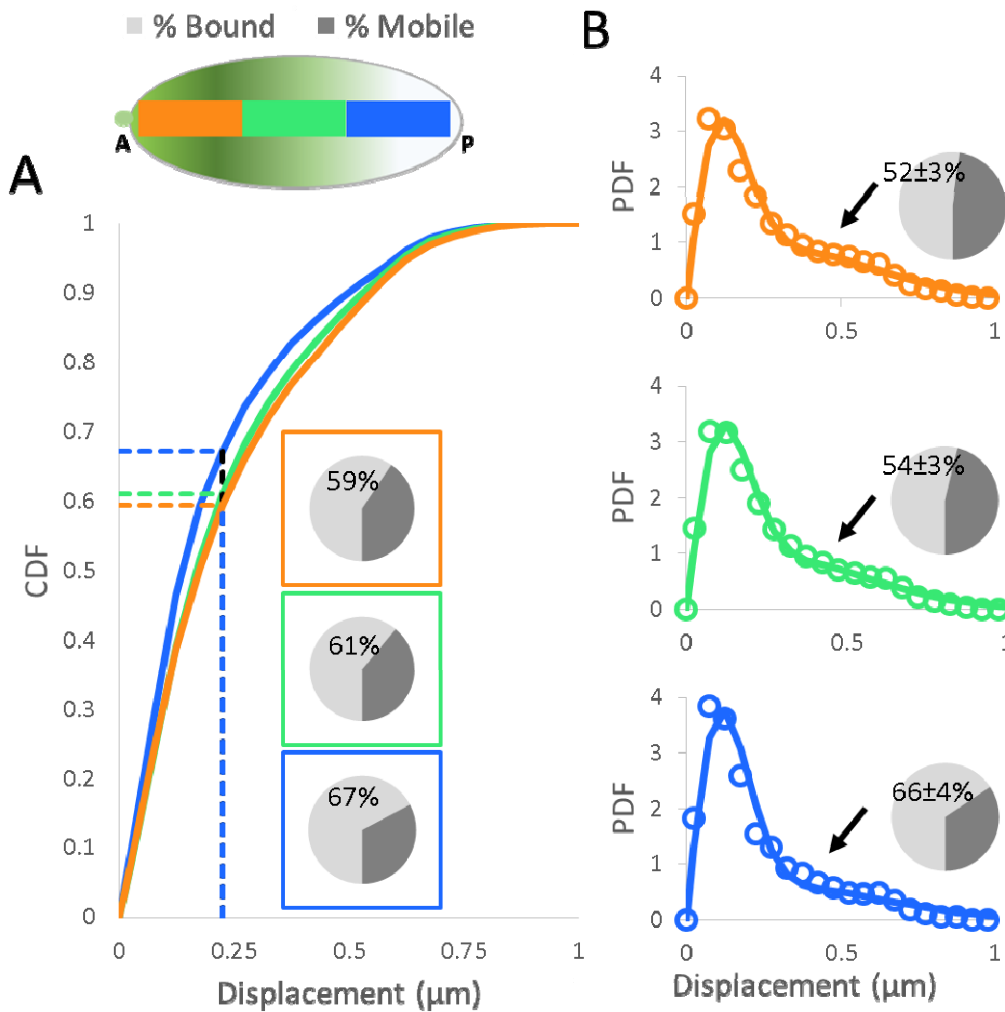
Figure 2- figure supplement 1. Analysis of Displacement Distributions (A) Cumulative

distribution functions of the displacement data, pie charts indicate the Bound and Mobile fraction

as measured by the CDF value at 0.225 µm (dashed lines). (B) Probability Density Function of

the displacement data (markers) and fits to the two population model (solid lines), pie charts

show the mobile and bound fractions from the results of the fit, labels indicate the bound fraction

and the error is the standard error associated with the fit parameter. Arrows point to the mobile

population in the distributions that is decreasing from anterior to posterior positions. (A-B) For

each position the following number of nuclei and trajectories were included in the analysis

802   Anterior: 30 nuclei, 12923, trajectories, Middle: 67 nuclei, 23640 trajectories, Posterior: 66
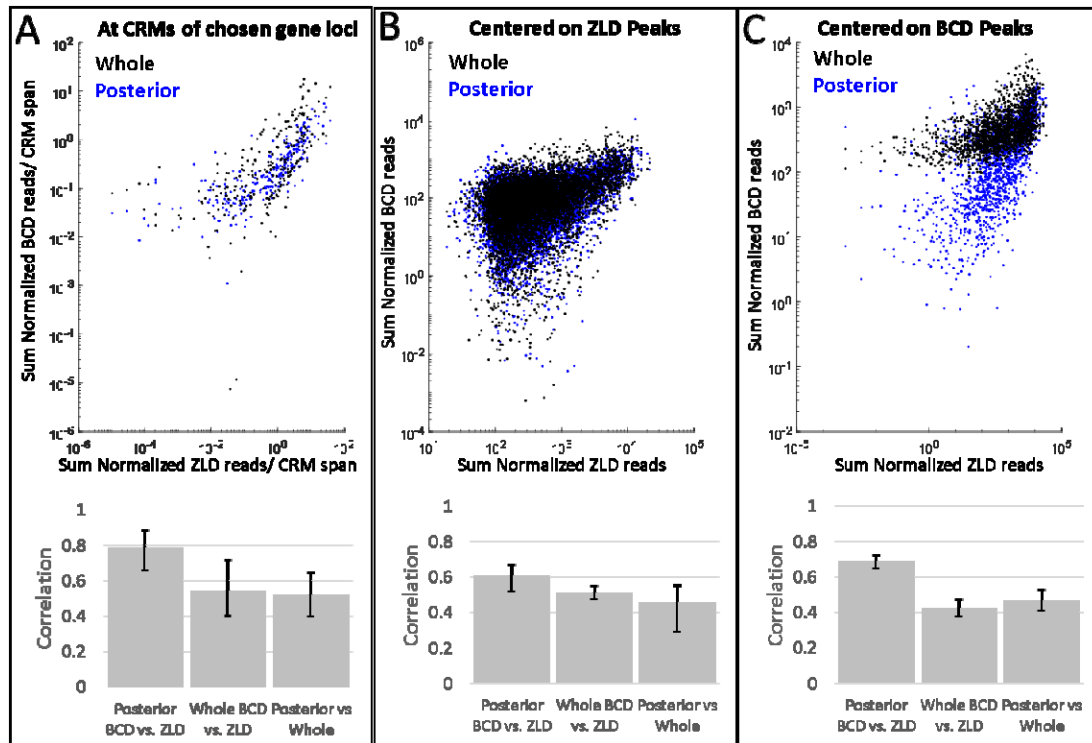
803   nuclei; 8600 trajectories.

804

805
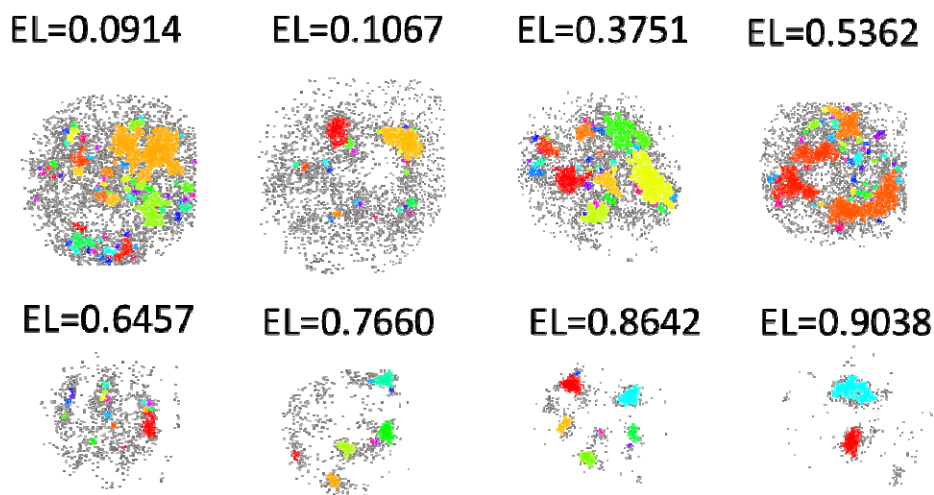
Figure 2- figure supplement 2. Cluster identification results from DBSCAN across the A-P axis. Examples of clusters identified along the A-P axis using DBSCAN with the position shown as fraction of embryonic length (EL). Particles included in the same clusters are represented with the same color.

810

Figure 3- figure supplement 1. BCD binding in whole and posterior thirds embryos compared to ZLD binding. (A) Sum of Normalized BCD ChIP-seq reads divided by the length of the respective CRMs for posterior thirds (blue) and whole embryo (black) vs. Sum of Normalized ZLD ChIP-seq reads divided by the length of the respective CRM at annotated cis-regulatory modules (CRMs) of *eve*, *giant*, *hunchback*, *knirps*, *hairy*, *kruppel*, *caudal*, *fushi-tarazu*, *engrailed*, *wingless*, *runt*, and *gooseberry* loci. A total of 293 CRMs from the RedFly database were analyzed. **(A-B)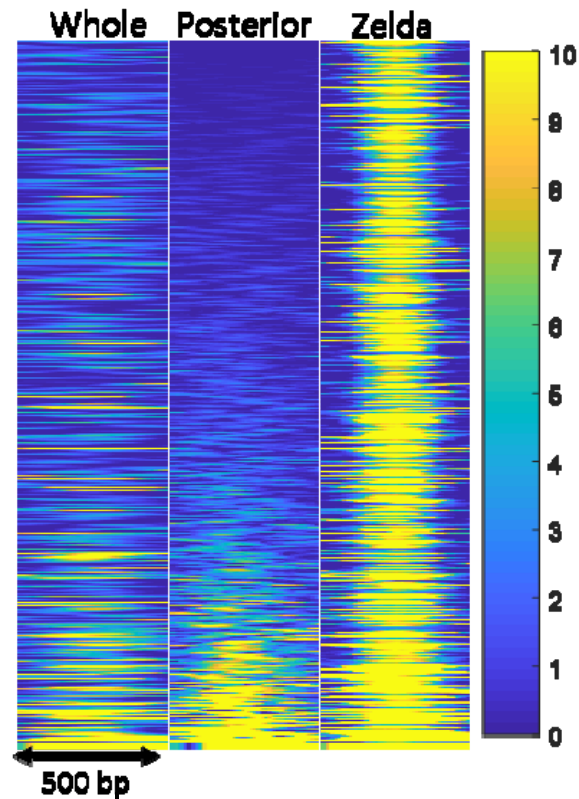** Sum of Normalized BCD ChIP-seq reads for posterior thirds (blue) and whole embryo (black) vs. Sum of Normalized ZLD ChIP-seq reads over a 500 bp region centered on **(B)** 8331 ZLD peaks and **(C)** 2145 BCD peaks. **(A-C)** Corresponding bar plots show Pearson correlation coefficients and error bars show 95% confidence intervals as determined by bootstrapping.
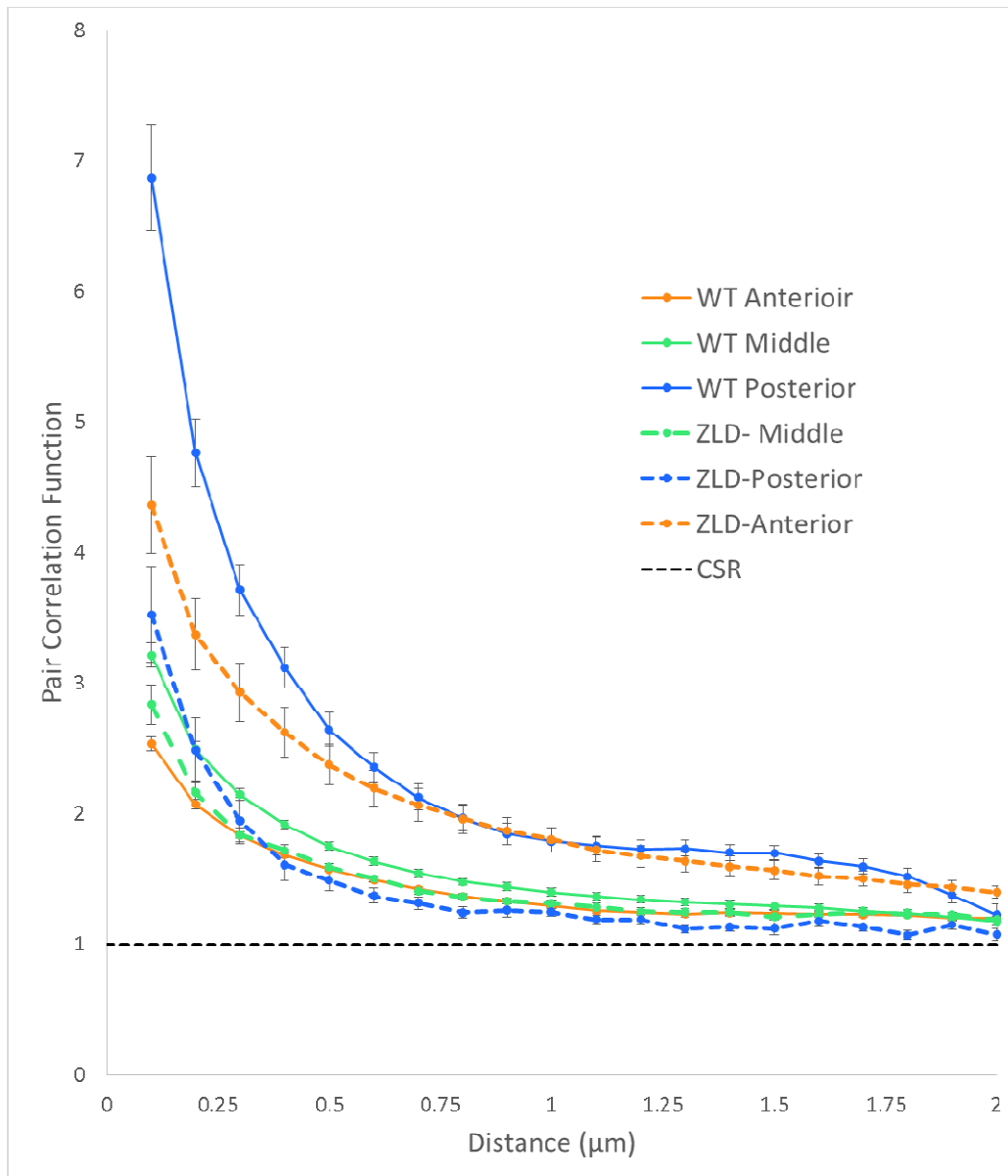
46

824

825 **Figure 3-figure supplement 2. BCD and ZLD binding at Zelda peaks.** Heat-map

826 representation of normalized ChIP-seq reads for BCD (1st two panels) and ZLD (3rd panel) in a

827 500 bp window centered on ZLD peaks sorted according to increasing BCD signal in the

828 posterior embryo data. A total of 8331 peaks are shown.

829

830

Figure 3- figure supplement 3. Averaged pair-correlation (radial distribution) functions for

nuclei in the WT and ZLD- cases. Black dashed line indicates complete spatial randomness

(CSR). Error bars indicate the standard error.

834

835 **VIDEO CAPTIONS**

836 **Video 1**-Movies corresponding to the still frames shown in Figure 1A.

837 **Video 2**- Representative data from a 90 second segment of a 100 millisecond exposure time

838 movie acquired at an anterior position (EL (x/L) of 0.1). Top left shows the raw data and top

839 right the corresponding surface plot representation. Bottom left shows a running max projection

840 of the data and bottom right shows a surface plot representation of the same

841 **Video 3**-Representative data acquired at 10 millisecond exposure times for 4 nuclei.